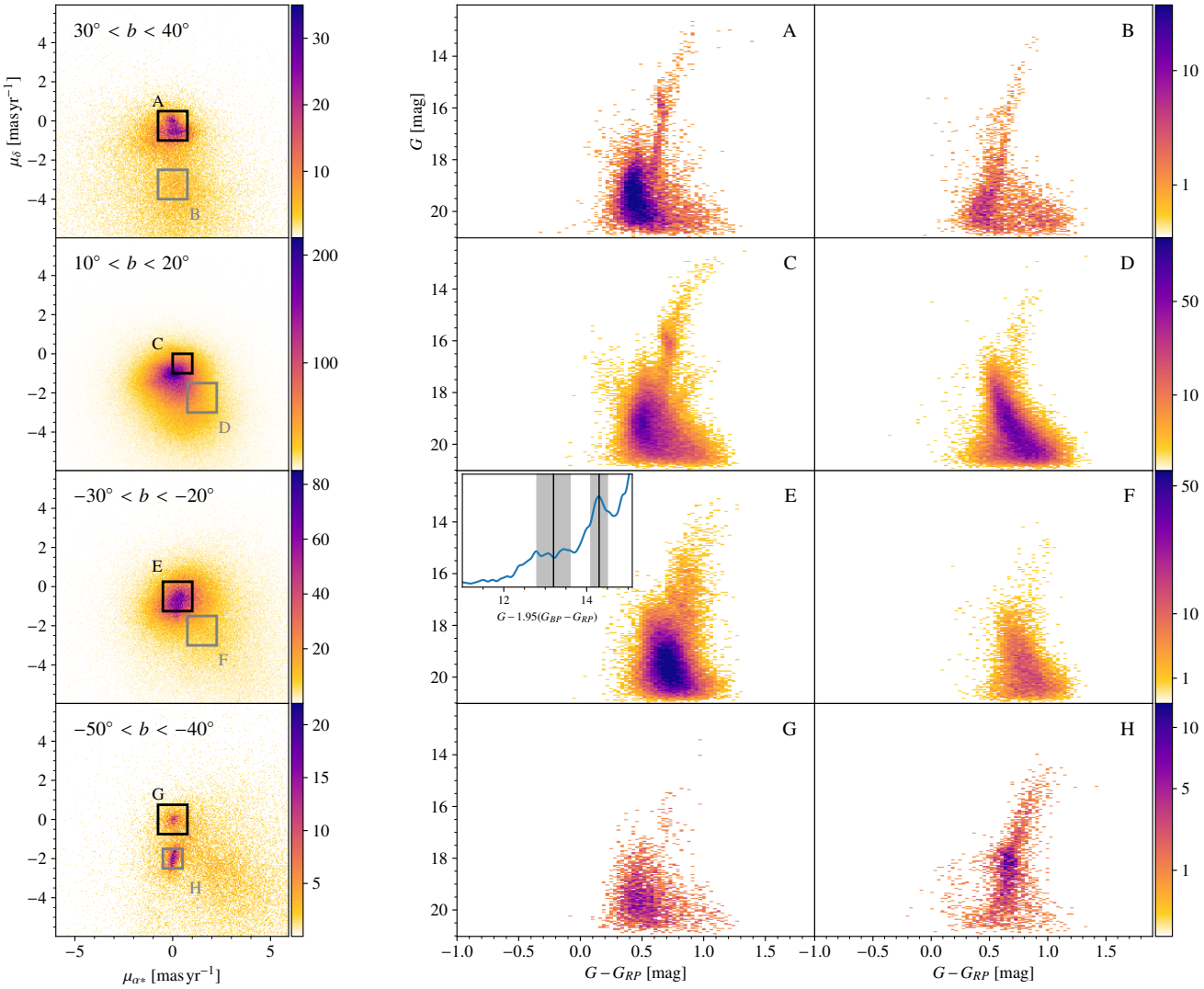

Fig. 21. Colour-magnitude diagrams of different features in the anticentre. The diagrams are for the kinematic groups selected in proper motion in the range $170° < \ell < 190°$. Each row corresponds to a different latitude. *First column*: distribution in proper motion and the definition of two regions of interested. The stellar population in these selections are shown in the *second and third columns*. We see structures such as ACS (A), Monoceros (C), the Sagittarius stream (H, C) and other outer disc structures (E).

(Ibata et al. 2003; Li et al. 2017), alternatively called south middle structure (Xu et al. 2015), at around ∼12 to 16 kpc from the Galactic centre. On the other hand, the faint RC could be related to TriAnd (Rocha-Pinto et al. 2004; Xu et al. 2015; Li et al. 2017; Bergemann et al. 2018), at a Galactocentric radius between 18 and 25. We note however that previous TriAnd detections were located around the range 100–160 deg in ℓ, thus not exactly in the anticentre direction, and our detection would then be a confirmation of the broadness of this structure and their extension up to $\ell = 180$, albeit predicted by models such as that from Sheffield et al. (2018).

6. Clusters in the outer disc

In this section, we investigate the peculiar clusters Berkeley 29 and Saurer 1. The *Gaia* EDR3 astrometric data allow us for the first time to perform a reliable member selection of these clusters and to constrain their proper motions in order to determine their orbits. We retained all sources brighter than $G = 19$ within 4 arcmin of the cluster centres. The members were identified from their *Gaia* proper motions and parallaxes with the unsupervised clustering procedure UPMASK (Krone-Martins & Moitinho 2014). Cantat-Gaudin et al. (2018), also using UPMASK, analysed the stars brighter than $G = 18$ mag of *Gaia* DR2 and detected Berkeley 29 but not Saurer 1. The improvement of *Gaia* EDR3 with respect to *Gaia* DR2 allows us to gain one magnitude and reliably detect both clusters. Figure 22 impressively shows how the stars in these clusters appear much more concentrated in proper motion space compared to DR2. The CMDs of the clusters are shown in Fig. 23, highlighting the sources that we consider the most secure members (with membership scores over 50%). We manually fitted PARSEC isochrones (Bressan et al. 2012) to the observed CMDs. For Berkeley 29 we employed an isochrone with a metallicity [Fe/H] = −0.5 (Yong et al. 2005; Cantat-Gaudin et al. 2016), an age $\log t = 9.55$, and a distance modulus of 15.5 mag with an extinction A_V of 0.2 mag. For Saurer 1 we used an isochrone of metallicity [Fe/H] = −0.4 (Carraro & Baume 2003;

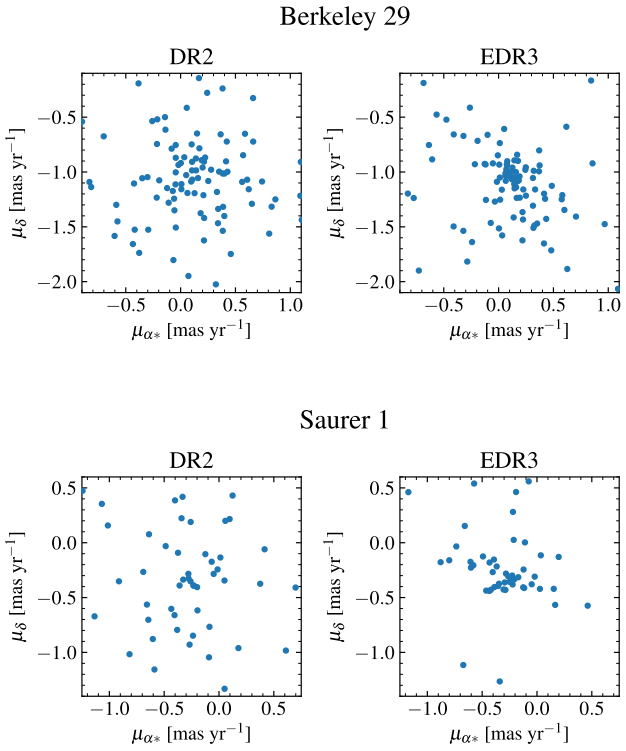

Fig. 22. Proper motions of the stars in Berkeley 29 and Saurer 1. The proper motions are for Berkeley 29 (*top*) and Saurer 1 (*bottom*) for *Gaia* DR2 (*left*) and *Gaia* EDR3 (*right*), for sources brighter than $G = 19$ in the investigated field of view. The reduced uncertainties in EDR3 make the stars appear much more clumped than in DR2, allowing for a better selection of members and a better determination of the proper motion of the clusters.

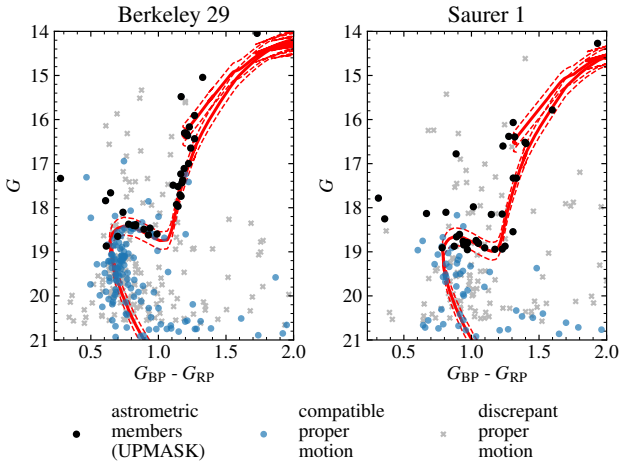

Fig. 23. CMDs for Berkeley 29 and Saurer 1. The secure members identified with UPMASK are indicated and used to compute the mean proper motions. The blue points are sources with similar proper motions but large uncertainties, or magnitudes $G > 19$. The red lines are PARSEC isochrones. The dashed lines correspond to offsets of ± 0.2 mag in distance modulus.

Cantat-Gaudin et al. 2016), an age $\log t = 9.6$, and a distance modulus of 15.4 mag with an extinction A_V of 0.4 mag.

The mean proper motions of the cluster members are $(\mu_{\alpha}*, \mu_\delta) = (0.11, -1.05)$ mas yr^{-1} for Berkeley 29, and $(-0.26, -0.32)$ mas yr^{-1} for Saurer 1. The mean tangential velocities V_ℓ and V_b (Eq. (4)) are represented in the first panel of Fig. 24, along with that of the Sagittarius stream particles from the Law & Majewski (2010) model. In this panel, all proper motions were corrected from the effect of the Solar motion. The velocity vector of both clusters is mostly parallel to the Galactic plane, and differs significantly from that of the stream.

We used `galpy` MWPotential2014 model (Bovy 2015) to integrate the orbits of these objects, shown in the left panels of Fig. 24. For this, we supplemented the quantities derived from *Gaia* data with line-of-sight velocities obtained from high-resolution spectra analysed by Cantat-Gaudin et al. (2016). Their mean line-of-sight velocities are 24.8 km s^{-1} for Berkeley 29 (from eight stars), and 98.0 km s^{-1} for Saurer 1 (from two stars). All the stars they used to compute those mean velocities are part of the sample of secure members we obtained in the present study. We estimated the uncertainty on the main orbital parameters by Monte-Carlo sampling of the uncertainties on the distance, line-of-sight velocity, and proper motion. We assumed an uncertainty of 0.2 mag on the distance modulus, and 2 km s^{-1} on the line-of-sight velocities of both clusters. The precision on the mean cluster proper motion is limited by systematics, on the level of 11 μas yr^{-1} on each component of the mean cluster proper motion. All sampled orbits correspond to prograde, bound trajectories. The maximum altitude above the Galactic plane is $z_{\max} = 1.80^{+0.45}_{-0.09}$ for Berkeley 29, and $z_{\max} = 1.59^{+0.11}_{-0.09}$ for Saurer 1. They also exhibit small eccentricities $e = 0.03^{+0.08}_{-0.01}$ and $0.05^{+0.06}_{-0.05}$, respectively. Despite their large Galactocentric distance, the orbits of these clusters are typical of disc objects. We obtained similar results with the model by McMillan (2017).

7. Discussion and conclusions

7.1. Summary of results

With the combination of photometric and astrometric data from *Gaia* EDR3, we explored the dynamics of different elements of the MW in the Galactic anticentre. The main results of this study are:

1. There are prominent oscillations in the median rotation and vertical velocities and dispersions of disc stars as a function of radius and angular momentum which depend on the evolutionary state of the stars (Sect. 4.1).
2. There are significant asymmetries in velocity when comparing stars above and below the standard Galactic plane for disc stars that can be as high as 5 km s^{-1} for the vertical velocities and 10 km s^{-1} for the rotation ones (Sect. 4.2).
3. At the outer disc, stars are predominantly following a bimodal distribution, with a group of stars mostly below the plane moving upwards with velocities of ~10 km s^{-1} and rotating faster by about ~30 km s^{-1} than another group of stars predominantly above the plane moving downwards by 2–5 km s^{-1} (Sect. 4.2).
4. The known R-V_ϕ ridges discovered with *Gaia* DR2, reach larger Galactocentric radius with EDR3 (up to 14 kpc) and there are also new ridges up to about 16–18 kpc, that is much beyond the limits reached in previous studies (Sect. 4.3).
5. Galactic rotation is detected as far as 18 kpc from the Galactic centre, being this a lower limit on the current thin disc size (Sects. 4.1 and 4.2).
6. The red sequence of high tangential velocity stars (suggested to be the ancient disc that was heated after the merger with *Gaia*-Enceladus-Sausage) now is seen to extend out to ~14 kpc (Sect. 5.1).

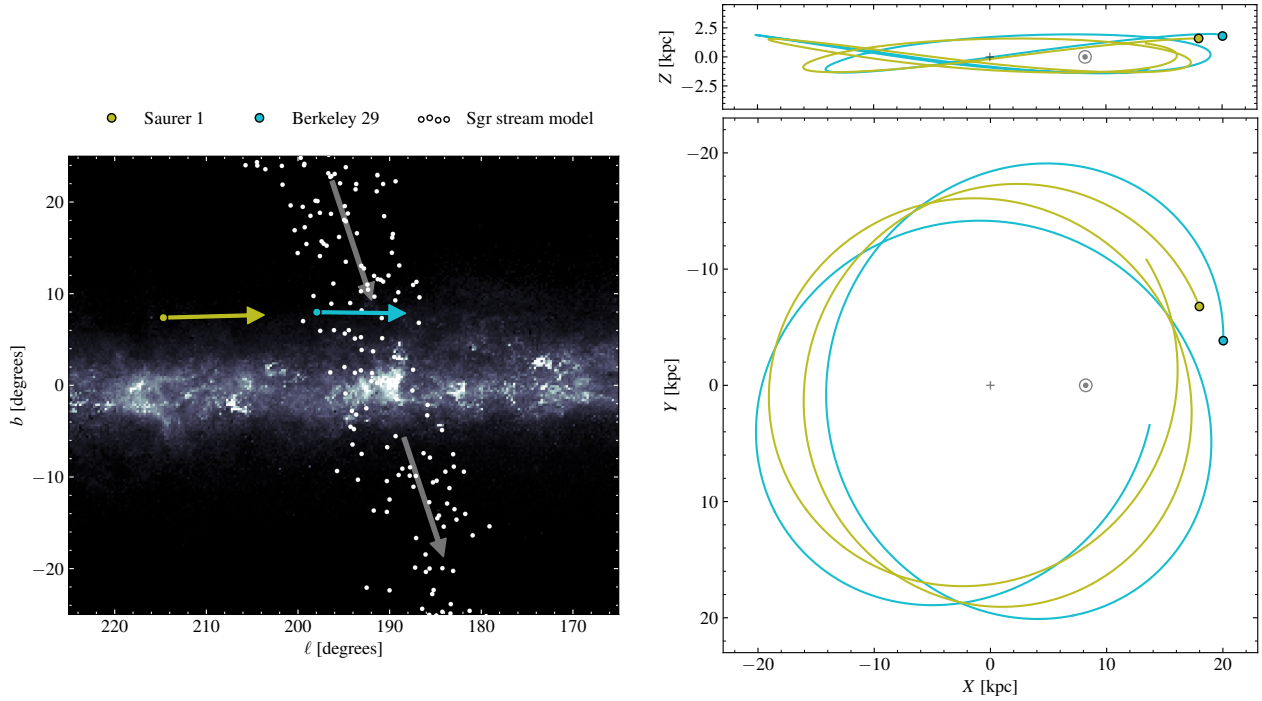

Fig. 24. Orbits if the Berkeley 29 and Saurer 1 clusters from EDR3 data. *Left*: location of Saurer 1 and Berkeley 29 in Galactic coordinates. The white symbols are the Sagittarius stream particles modelled by Law & Majewski (2010). The arrows indicate mean tangential velocities corrected for the solar motion (V_ℓ, V_b). The background is the integrated extinction model of Green et al. (2015), beyond 2 kpc. *Right*: integrated orbits of Saurer 1 and Berkeley 29. The Sun's position and Galactic centre are indicated as the usual Sun's symbol and cross, respectively. We find that the orbits of these clusters are very similar and typical of the disc.

7. The blue sequence (assumed to be the debris of the *Gaia*-Enceladus-Sausage) is much more extended and can be detected at least beyond 17 kpc (Sect. 5.1).
8. The far anticentre shows a intricate superposition of structures in the proper motion and photometry diagrams including the leading (in the north) and trailing (in the south) Sagittarius stream, and known outer disc structures such of Monoceros and ACS in the north (Sect. 5.2).
9. There are two structures at latitudes of $-30 < b < -20$ deg approximately at 9 and 14 kpc from the Sun, tentatively related to the Monoceros in the south and an extension of TriAnd in the anticentre direction, respectively (Sect. 5.2).
10. The clusters Berkeley 29 and Saurer 1, which are among the oldest open clusters known, are found to be on disc-like orbits despite being located at around 20 kpc from the Galactic centre (Sect. 6).

7.2. Discussion (I): MW disc dynamics

As in *Gaia* DR2, the disc is found to be rather complex. Nearby, the rotation velocities are dominated by the known ridges in the (R, V^*_ϕ) plane, which are now detected up to 14 kpc from the Galactic centre, that is 3 kpc farther than for DR2, while two additional ridges are discovered that reach 16–18 kpc. The overlap of distinct ridges in R seems to be the cause of some oscillation seen in the rotation curve, as already suggested by Martinez-Medina et al. (2019), although they could also be related to the physical location of the spiral arms (Sancisi 2004; McGaugh 2019), rather than their resonances (Barros et al. 2013).

The most prominent nearby ridge is Sirius, followed by the hat, L18, Hyades and Hercules. If indeed the Hercules, Sirius and hat ridges are signatures of the corotation, 4:1, and 2:1 Outer Lindblad Resonance of the bar (Monari et al. 2019; Laporte et al. 2020a), respectively, there could be the 4:3 and 1:1 resonances beyond that (see Kawata et al. 2020) but perhaps there is a different explanation for the new ridges beyond 12 kpc discovered here, either spiral structure (with a lower pattern speed or transient) or the perturbation from Sagittarius (or the two at the same time since perturbations from satellites inevitably induce density spirals and rings, Purcell et al. 2011).

The *Gaia* EDR3 now allows for a full characterisation of the velocity ellipsoid and the asymmetric drift as a function of age and radius. We see clear oscillations in V^*_Z with radius (and angular momentum) of an amplitude of 1–2 km s^{-1} but increasing for younger stars. As already noticed before (e.g. Schönrich & Dehnen 2018; Huang et al. 2018; Beane et al. 2019; Cheng et al. 2020) but now seen at a higher precision with *Gaia* EDR3, these oscillations could indicate a vertical wave propagating radially and are possibly associated to oscillations in the local mid-plane itself. The vertical velocity dispersions do not show the expected decreasing behaviour with radius but seem to be flat or increase and present very prominent oscillations that appear connected to the oscillations in the median velocities.

In the outer disc ($R > 12$ kpc), the velocity field is dominated by an upwards motion of about 5 km s^{-1}. Already seen in Gaia Collaboration (2018c), Wang et al. (2018), Poggio et al. (2018), Romero-Gómez et al. (2019), Carrillo et al. (2019), López-Corredoira et al. (2020) and Cheng et al. (2020), it has been associated to the warp that in the anticentre is near the line-of nodes, a bending wave due to Sagittarius, or to a disc that never achieved equilibrium. Here, however, we go one step beyond and find, coexisting in R, a bimodal distribution of stars moving vertically with opposite directions and with a different

amount of rotation. The feature can be observed also as a vertical velocity oscillation in angular momentum space, which can thus have different phases coexisting at the same R. This bimodality shows similar phase space correlations to those of the phase spiral (Antoja et al. 2018). Each group of the bimodality could be interpreted as different wraps of a phase-mixing feature or a combination of bending waves. Missing data in this study such as line-of-sight velocities and chemistry will help in the understanding of this feature. The WEAVE Galactic Archaeology survey (Dalton et al. 2016; Famaey et al. 2016) has a dedicated science case in the region of the anticentre to obtain line-of-sight velocities in complement to *Gaia*, which will be crucial in this and many other aspects explored in this study. Yet our exploration reveals that simple 2d projections of phase space often do not capture the full complexity of the disc dynamics: when the vertical velocities are explored alone as a function of radius, only the upward motion (as in previous studies) is seen and adding more coordinates is necessary to observe this bimodality.

To interpret the complex patterns observed, a dynamical framework is required that no longer assumes decoupling between the vertical and horizontal movements (D'Onghia et al. 2016) and is capable of linking the small scale features such as the ridges, the global streaming motions, the phase spiral and perhaps structures such as the warp, the flare and the spiral arms. In any case, we probably live in a Galaxy with a highly perturbed outer disc (e.g. Widrow et al. 2012; Wang et al. 2017; Antoja et al. 2018; Beane et al. 2019) as seen in simulations of MW-like galaxies perturbed by a Sagittarius-like galaxy (Purcell et al. 2011; Gómez et al. 2013, 2017; Laporte et al. 2018) having rings with non-null vertical velocities, qualitatively comparable to what we find here.

7.3. Discussion (II): MW constituents

After *Gaia* DR2, our understanding of the Galactic components has changed, in particular recognising that most of the (local) halo is made of debris from a single accretion event (forming a blue sequence in the HR diagram of high transverse velocity stars) and that we here find to be extended beyond the local neighbourhood at least up to distances of 17 kpc from the Galactic centre. This is consistent with expectations from, for example, the orbit integrations of Deason et al. (2018), but also emphasises the global importance of the debris. The redder component of the HR diagram does not extend this far, having very few stars already around 14 kpc. If this redder component is the heated thick disc after the merger (as claimed in Helmi et al. 2018; Di Matteo et al. 2019; Gallart et al. 2019; Belokurov et al. 2020), this would imply that it is more compact than the canonical thick disc, which can be detected up to this radius. It will be interesting to try to constrain its initial properties, particularly through comparison to simulations of mergers and subsequent disc growth.

In line with Carraro et al. (2010) and López-Corredoira et al. (2018) that advocate a disc larger than the previously thought 12–14 kpc (Minniti et al. 2011, and references therein), we find evidence of circular rotation up to about 18 kpc from the Galactic centre. A more precise value for such an important measurement needs a detailed analysis of the effects of the adopted zero parallax point, the biases on any distance estimate (see Appendices C and D) and aspects such as the flare (e.g. López-Corredoira & Molgó 2014). We compared the effects of a constant parallax offset of $-17\,\mu$as (the average offset of the quasars) with that of Lindegren et al. (2021a) – a more sophisticated prescription as a function of magnitude, colour and ecliptic latitude. We find that the latter gives a more compressed distance scale (that propagates to velocities) but at this point it is not straightforward to claim that one prescription is better than the other (Lindegren et al. 2021a). In any case, the features observed remain qualitatively the same regardless of the zero point.

Gaia has also provided us with a window into the structures that dwell at the edge of the disc. We detected the Monoceros and the ACS above the disc plane and other structures in the south. Our southern detections are possibly related to the Monoceros south or south middle structure (e.g. Ibata et al. 2003; Xu et al. 2015) and TriAnd (Rocha-Pinto et al. 2004), which have not been probed in detail at $\ell \sim 180$ deg so far due to the high extinction (e.g. Slater et al. 2014; Xu et al. 2015). If confirmed, this would be the first TriAnd detection with *Gaia* data (but see Ramos et al. 2021) and the first time it is observed beyond its previously known longitude limit of $\ell \sim 160$ deg. Curiously, the part of the disc bimodality of stars below the plane moving upwards strongly at 12 kpc coincides in distance with this nearby southern structure, though the latter is at a lower latitude. The connection between these features certainly needs some attention. Whether these structures are the corresponding northern and southern counterparts of the vertically oscillating disc (bending wave) expected in the scenario proposed by Widrow et al. (2012) and Yanny & Gardner (2013), or they are individual rings or feather structures in the outermost parts of the disc as suggested in Ibata et al. (2003), Kazantzidis et al. (2008), Purcell et al. (2011), Gómez et al. (2013) and Laporte et al. (2019b) also remains undetermined. In any case, future studies can benefit from the *Gaia* data that enable the kinematic selection of members of these features, providing a uniform sample of all the stellar types, and the determination of their proper motion.

Here we looked at two particular clusters, Berkeley 29 and Saurer 1, that due to their great distances from the Galaxy centre (around 20 kpc, derived photometrically and thus not affected by the parallax offset) and their old age (3–4 Gyr) probe extreme conditions in the Galaxy. Using an improved membership assignation and the better astrometry of *Gaia* EDR3, we ascertain that the two clusters are on disc orbits, unlike what was claimed by previous studies (Frinchaboy 2006; Wu et al. 2009; Carraro et al. 2007; Vande Putte et al. 2010; Carraro & Bensby 2009). Yet, their distant location makes us wonder whether the disc extends to such a distance or whether these clusters were brought there by other means (radial migration, interaction with a satellite, expelled material from the disc). In particular Berkeley 29 has been already associated to Monoceros in Carraro et al. (2004) and in Frinchaboy et al. (2004), though in the latter case advocating for a stream origin. Our distances and proper motion of these clusters are compatible with the ones of Monoceros. Similarly, after examining the literature (Rocha-Pinto et al. 2004; Li et al. 2012; Cantat-Gaudin et al. 2016; Sheffield et al. 2018), we note that their chemistry and line-of-sight velocity are also broadly comparable. These clusters thus can be small but relevant pieces of information on the outer disc unknowns.

7.4. Conclusion

The quality of the EDR3 *Gaia* data together with the advantage of having astrometry and photometry from the same mission have allowed us to extend the horizon for exploration towards the very end of the disc, travel to the past to explore its ancient components and detect its small constituents and phase space

features with better resolution. With a simple exploration of the *Gaia* data we find new complex patterns of movement in the outskirts of the Galactic disc, we estimate the extent of the ancient MW disc, show how the anticentre is a crossroad of structures likely both of internal and external origin, and uncover the nature of the orbits of two distant clusters. The anticentre is thus proven to be an excellent testbed region in the quest of deciphering the structure and history of our Galaxy that many astrophysicists are pursuing in the *Gaia* era.

Acknowledgements. We thank the referee Dr. James Binney for his comments. This work has made use of data from the European Space Agency (ESA) mission *Gaia* (https://www.cosmos.esa.int/gaia), processed by the *Gaia* Data Processing and Analysis Consortium (DPAC, https://www.cosmos.esa.int/web/gaia/dpac/consortium). Funding for the DPAC has been provided by national institutions, in particular the institutions participating in the *Gaia* Multilateral Agreement. This work presents results from the European Space Agency (ESA) space mission *Gaia*. *Gaia* data are being processed by the *Gaia* Data Processing and Analysis Consortium (DPAC). Funding for the DPAC is provided by national institutions, in particular the institutions participating in the *Gaia* MultiLateral Agreement (MLA). The *Gaia* mission website is https://www.cosmos.esa.int/gaia. The *Gaia* archive website is https://archives.esac.esa.int/gaia. The *Gaia* mission and data processing have financially been supported by, in alphabetical order by country: the Algerian Centre de Recherche en Astronomie, Astrophysique et Géophysique of Bouzareah Observatory; the Austrian Fonds zur Förderung der wissenschaftlichen Forschung (FWF) Hertha Firnberg Programme through grants T359, P20046, and P23737; the BELgian federal Science Policy Office (BELSPO) through various PROgramme de Développement d'Expériences scientifiques (PRODEX) grants and the Polish Academy of Sciences - Fonds Wetenschappelijk Onderzoek through grant VS.091.16N, and the Fonds de la Recherche Scientifique (FNRS); the Brazil-France exchange programmes Fundação de Amparo à Pesquisa do Estado de São Paulo (FAPESP) and Coordenação de Aperfeicoamento de Pessoal de Nível Superior (CAPES) - Comité Français d'Evaluation de la Coopération Universitaire et Scientifique avec le Brésil (COFECUB); the National Science Foundation of China (NSFC) through grants 11573054 and 11703065 and the China Scholarship Council through grant 201806040200; the Tenure Track Pilot Programme of the Croatian Science Foundation and the École Polytechnique Fédérale de Lausanne and the project TTP-2018-07-1171 'Mining the Variable Sky', with the funds of the Croatian-Swiss Research Programme; the Czech-Republic Ministry of Education, Youth, and Sports through grant LG 15010 and INTER-EXCELLENCE grant LTAUSA18093, and the Czech Space Office through ESA PECS contract 98058; the Danish Ministry of Science; the Estonian Ministry of Education and Research through grant IUT40-1; the European Commission's Sixth Framework Programme through the European Leadership in Space Astrometry (ELSA) Marie Curie Research Training Network (MRTN-CT-2006-033481), through Marie Curie project PIOF-GA-2009-255267 (Space AsteroSeismology and RR Lyrae stars, SAS-RRL), and through a Marie Curie Transfer-of-Knowledge (ToK) fellowship (MTKD-CT-2004-014188); the European Commission's Seventh Framework Programme through grant FP7-606740 (FP7-SPACE-2013-1) for the *Gaia* European Network for Improved data User Services (GENIUS) and through grant 264895 for the *Gaia* Research for European Astronomy Training (GREAT-ITN) network; the European Research Council (ERC) through grants 320360 and 647208 and through the European Union's Horizon 2020 research and innovation and excellent science programmes through Marie Skłodowska-Curie grant 745617 as well as grants 670519 (Mixing and Angular Momentum tranSport of massIvE stars – MAMSIE), 687378 (Small Bodies: Near and Far), 682115 (Using the Magellanic Clouds to Understand the Interaction of Galaxies), and 695099 (A sub-percent distance scale from binaries and Cepheids – CepBin); the European Science Foundation (ESF), in the framework of the *Gaia* Research for European Astronomy Training Research Network Programme (GREAT-ESF); the European Space Agency (ESA) in the framework of the *Gaia* project, through the Plan for European Cooperating States (PECS) programme through grants for Slovenia, through contracts C98090 and 4000106398/12/NL/KML for Hungary, and through contract 4000115263/15/NL/IB for Germany; the Academy of Finland and the Magnus Ehrnrooth Foundation; the French Centre National d'Etudes Spatiales (CNES), the Agence Nationale de la Recherche (ANR) through grant ANR-10-IDEX-0001-02 for the 'Investissements d'avenir' programme, through grant ANR-15-CE31-0007 for project 'Modelling the Milky Way in the *Gaia* era' (MOD4Gaia), through grant ANR-14-CE33-0014-01 for project 'The Milky Way disc formation in the *Gaia* era' (ARCHEOGAL), and through grant ANR-15-CE31-0012-01 for project 'Unlocking the potential of Cepheids as primary distance calibrators' (UnlockCepheids), the Centre National de la Recherche Scientifique (CNRS) and its SNO *Gaia* of the Institut des Sciences de l'Univers (INSU), the 'Action Fédératrice *Gaia*' of the Observatoire de Paris, the Région de Franche-Comté, and the Programme National de Gravitation, Références, Astronomie, et Métrologie (GRAM) of CNRS/INSU with the Institut National Polytechnique (INP) and the Institut National de Physique nucléaire et de Physique des Particules (IN2P3) co-funded by CNES; the German Aerospace Agency (Deutsches Zentrum für Luft- und Raumfahrt e.V., DLR) through grants 50QG0501, 50QG0601, 50QG0602, 50QG0701, 50QG0901, 50QG1001, 50QG1101, 50QG1401, 50QG1402, 50QG1403, 50QG1404, and 50QG1904 and the Centre for Information Services and High Performance Computing (ZIH) at the Technische Universität (TU) Dresden for generous allocations of computer time; the Hungarian Academy of Sciences through the Lendület Programme grants LP2014-17 and LP2018-7 and through the Premium Postdoctoral Research Programme (L. Molnár), and the Hungarian National Research, Development, and Innovation Office (NKFIH) through grant KH_18-130405; the Science Foundation Ireland (SFI) through a Royal Society – SFI University Research Fellowship (M. Fraser); the Israel Science Foundation (ISF) through grant 848/16; the Agenzia Spaziale Italiana (ASI) through contracts I/037/08/0, I/058/10/0, 2014-025-R.0, 2014-025-R.1.2015, and 2018-24-HH.0 to the Italian Istituto Nazionale di Astrofisica (INAF), contract 2014-049-R.0/1/2 to INAF for the Space Science Data Centre (SSDC, formerly known as the ASI Science Data Center, ASDC), contracts I/008/10/0, 2013/030/I.0, 2013-030-I.0.1-2015, and 2016-17-I.0 to the Aerospace Logistics Technology Engineering Company (ALTEC S.p.A.), INAF, and the Italian Ministry of Education, University, and Research (Ministero dell'Istruzione, dell'Università e della Ricerca) through the Premiale project 'MIning The Cosmos Big Data and Innovative Italian Technology for Frontier Astrophysics and Cosmology' (MITiC); the Netherlands Organisation for Scientific Research (NWO) through grant NWO-M-614.061.414, through a VICI grant (A. Helmi), and through a Spinoza prize (A. Helmi), and the Netherlands Research School for Astronomy (NOVA); the Polish National Science Centre through HARMONIA grant 2018/30/M/ST9/00311, DAINA grant 2017/27/L/ST9/03221, and PRELUDIUM grant 2017/25/N/ST9/01253, and the Ministry of Science and Higher Education (MNiSW) through grant DIR/WK/2018/12; the Portugese Fundação para a Ciência e a Tecnologia (FCT) through grants SFRH/BPD/74697/2010 and SFRH/BD/128840/2017 and the Strategic Programme UID/FIS/00099/2019 for CENTRA; the Slovenian Research Agency through grant P1-0188; the Spanish Ministry of Economy (MINECO/FEDER, UE) through grants ESP2016-80079-C2-1-R, ESP2016-80079-C2-2-R, RTI2018-095076-B-C21, RTI2018-095076-B-C22, BES-2016-078499, and BES-2017-083126 and the Juan de la Cierva formación 2015 grant FJCI-2015-2671, the Spanish Ministry of Education, Culture, and Sports through grant FPU16/03827, the Spanish Ministry of Science and Innovation (MICINN) through grant AYA2017-89841P for project 'Estudio de las propiedades de los fósiles estelares en el entorno del Grupo Local' and through grant TIN2015-65316-P for project 'Computación de Altas Prestaciones VII', the Severo Ochoa Centre of Excellence Programme of the Spanish Government through grant SEV2015-0493, the Institute of Cosmos Sciences University of Barcelona (ICCUB, Unidad de Excelencia 'María de Maeztu') through grants MDM-2014-0369 and CEX2019-000918-M, the University of Barcelona's official doctoral programme for the development of an R+D+i project through an Ajuts de Personal Investigador en Formació (APIF) grant, the Spanish Virtual Observatory through project AyA2017-84089, the Galician Regional Government, Xunta de Galicia, through grants ED431B-2018/42 and ED481A-2019/155, support received from the Centro de Investigación en Tecnologías de la Información y las Comunicaciones (CITIC) funded by the Xunta de Galicia, the Xunta de Galicia and the Centros Singulares de Investigación de Galicia for the period 2016-2019 through CITIC, the European Union through the European Regional Development Fund (ERDF) / Fondo Europeo de Desenvolvemento Rexional (FEDER) for the Galicia 2014-2020 Programme through grant ED431G-2019/01, the Red Española de Supercomputación (RES) computer resources at MareNostrum, the Barcelona Supercomputing Centre - Centro Nacional de Supercomputación (BSC-CNS) through activities AECT-2016-1-0006, AECT-2016-2-0013, AECT-2016-3-0011, and AECT-2017-1-0020, the Departament d'Innovació, Universitats i Empresa de la Generalitat de Catalunya through grant 2014-SGR-1051 for project 'Models de Programació i Entorns d'Execució Parallels' (MPEXPAR), and Ramon y Cajal Fellowship RYC2018-025968-I; the Swedish National Space Agency (SNSA/Rymdstyrelsen); the Swiss State Secretariat for Education, Research, and Innovation through the ESA PRODEX programme, the Mesures d'Accompagnement, the Swiss Activités Nationales Complémentaires, and the Swiss National Science Foundation; the United Kingdom Particle Physics and Astronomy Research Council (PPARC), the United Kingdom Science and Technology Facilities Council (STFC), and the United Kingdom Space Agency (UKSA) through the following grants to the University of Bristol, the University of Cambridge, the University of Edinburgh, the University of Leicester, the Mullard Space Sciences Laboratory of University College London, and the United Kingdom Rutherford Appleton Laboratory (RAL): PP/D006511/1, PP/D006546/1, PP/D006570/1, ST/I000852/1, ST/J005045/1, ST/K00056X/1, ST/K000209/1, ST/K000756/1, ST/L006561/1, ST/N000595/1, ST/N000641/1, ST/N000978/1, ST/N001117/1, ST/S000089/1, ST/S000976/1, ST/S001123/1, ST/S001948/1, ST/S002103/1, and ST/V000969/1.

References

Ahumada, R., Allende Prieto, C., Almeida, A., et al. 2020, ApJS, 249, 3
Antoja, T., Figueras, F., Fernández, D., & Torra, J. 2008, A&A, 490, 135
Antoja, T., de Bruijne, J., Figueras, F., et al. 2017, A&A, 602, L13
Antoja, T., Helmi, A., Romero-Gómez, M., et al. 2018, Nature, 561, 360
Antoja, T., Ramos, P., Mateu, C., et al. 2020, A&A, 635, L3
Aumer, M., & Binney, J. J. 2009, MNRAS, 397, 1286
Bailer-Jones, C. A. L. 2015, PASP, 127, 994
Bailer-Jones, C. A. L., Rybizki, J., Fouesneau, M., Mantelet, G., & Andrae, R. 2018, AJ, 156, 58
Barros, D. A., Lépine, J. R. D., & Junqueira, T. C. 2013, MNRAS, 435, 2299
Beane, A., Sanderson, R. E., Ness, M. K., et al. 2019, ApJ, 883, 103
Belokurov, V., Erkal, D., Evans, N. W., Koposov, S. E., & Deason, A. J. 2018, MNRAS, 478, 611
Belokurov, V., Sanders, J. L., Fattahi, A., et al. 2020, MNRAS, 494, 3880
Bennett, M., & Bovy, J. 2019, MNRAS, 482, 1417
Bergemann, M., Sesar, B., Cohen, J. G., et al. 2018, Nature, 555, 334
Binney, J., & Schönrich, R. 2018, MNRAS, 481, 1501
Binney, J., & Tremaine, S. 2008, Galactic Dynamics, 2nd edn. (Princeton: Princeton University Press)
Binney, J., Gerhard, O. E., Stark, A. A., Bally, J., & Uchida, K. I. 1991, MNRAS, 252, 210
Bland-Hawthorn, J., & Gerhard, O. 2016, ARA&A, 54, 529
Bland-Hawthorn, J., Sharma, S., Tepper-Garcia, T., et al. 2019, MNRAS, 486, 1167
Blitz, L., & Spergel, D. N. 1991, ApJ, 379, 631
Boubert, D., & Everall, A. 2020, MNRAS, 497, 4246
Bovy, J. 2015, ApJS, 216, 29
Bragaglia, A., & Tosi, M. 2006, AJ, 131, 1544
Bressan, A., Marigo, P., Girardi, L., et al. 2012, MNRAS, 427, 127
Cantat-Gaudin, T., Donati, P., Vallenari, A., et al. 2016, A&A, 588, A120
Cantat-Gaudin, T., Jordi, C., Vallenari, A., et al. 2018, A&A, 618, A93
Cardelli, J. A., Clayton, G. C., & Mathis, J. S. 1989, ApJ, 345, 245
Carlin, J. L., DeLaunay, J., Newberg, H. J., et al. 2013, ApJ, 777, L5
Carraro, G., & Baume, G. 2003, MNRAS, 346, 18
Carraro, G., & Bensby, T. 2009, MNRAS, 397, L106
Carraro, G., Bresolin, F., Villanova, S., et al. 2004, AJ, 128, 1676
Carraro, G., Geisler, D., Villanova, S., Frinchaboy, P. M., & Majewski, S. R. 2007, A&A, 476, 217
Carraro, G., Vázquez, R. A., Costa, E., Perren, G., & Moitinho, A. 2010, ApJ, 718, 683
Carrillo, I., Minchev, I., Steinmetz, M., et al. 2019, MNRAS, 490, 797
Casagrande, L., & VandenBerg, D. A. 2018, MNRAS, 479, L102
Cheng, X., Anguiano, B., Majewski, S. R., et al. 2020, ApJ, 905, 49
Crane, J. D., Majewski, S. R., Rocha-Pinto, H. J., et al. 2003, ApJ, 594, L119
Dalton, G., Trager, S., Abrams, D. C., et al. 2016, SPIE Conf. Ser., 9908, 99081G
Deason, A. J., Belokurov, V., Koposov, S. E., & Lancaster, L. 2018, ApJ, 862, L1
de Boer, T. J. L., Belokurov, V., & Koposov, S. E. 2018, MNRAS, 473, 647
Dehnen, W. 1998, AJ, 115, 2384
de Vaucouleurs, G. 1964, IAU Symp., 20, 195
Di Matteo, P., Haywood, M., Lehnert, M. D., et al. 2019, A&A, 632, A4
D'Onghia, E., Madau, P., Vera-Ciro, C., Quillen, A., & Hernquist, L. 2016, ApJ, 823, 4
Drimmel, R., & Spergel, D. N. 2001, ApJ, 556, 181
Fabricius, C., Luri, X., Arenou, F., et al. 2021, A&A, 649, A5 (*Gaia* EDR3 SI)
Famaey, B., Jorissen, A., Luri, X., et al. 2005, A&A, 430, 165
Famaey, B., Antoja, T., Romero-Gomez, M., et al. 2016, SF2A-2016: Proceedings of the Annual meeting of the French Society of Astronomy and Astrophysics, eds. C. Reylé, J. Richard, L. Cambrésy, M. Deleuil, E. Pécontal, L. Tresse, & I. Vauglin, 281
Fragkoudi, F., Katz, D., Trick, W., et al. 2019, MNRAS, 488, 3324
Frinchaboy, P. M. 2006, ArXiv e-prints, [arXiv:astro-ph/0604133]
Frinchaboy, P. M., & Phelps, R. L. 2002, AJ, 123, 2552
Frinchaboy, P. M., Majewski, S. R., Crane, J. D., et al. 2004, ApJ, 602, L21
Friske, J. K. S., & Schönrich, R. 2019, MNRAS, 490, 5414
Gaia Collaboration (Prusti, T., et al.) 2016, A&A, 595, A1
Gaia Collaboration (Babusiaux, C., et al.) 2018a, A&A, 616, A10
Gaia Collaboration (Brown, A. G. A., et al.) 2018b, A&A, 616, A1
Gaia Collaboration (Katz, D., et al.) 2018c, A&A, 616, A11
Gaia Collaboration (Brown, A. G. A., et al.) 2021a, A&A, 649, A1 (*Gaia* EDR3 SI)
Gaia Collaboration (Klioner, S. A., et al.) 2021b, A&A, 649, A9 (*Gaia* EDR3 SI)
Gaia Collaboration (Luri, X., et al.) 2021c, A&A, 649, A7 (*Gaia* EDR3 SI)
Gaia Collaboration (Smart, R. L., et al.) 2021d, A&A, 649, A6 (*Gaia* EDR3 SI)
Gallart, C., Bernard, E. J., Brook, C. B., et al. 2019, Nat. Astron., 407
Gómez, F. A., Minchev, I., O'Shea, B. W., et al. 2013, MNRAS, 429, 159
Gómez, F. A., White, S. D. M., Grand , R. J. J., et al. 2017, MNRAS, 465, 3446
GRAVITY Collaboration (Abuter, R., et al.) 2019, A&A, 625, L10
Green, G. M., Schlafly, E. F., Finkbeiner, D. P., et al. 2015, ApJ, 810, 25
Green, G. M., Schlafly, E., Zucker, C., Speagle, J. S., & Finkbeiner, D. 2019, ApJ, 887, 93
Grillmair, C. J. 2006, ApJ, 651, L29
Hawkins, K., Leistedt, B., Bovy, J., & Hogg, D. W. 2017, MNRAS, 471, 722
Helmi, A., White, S. D. M., de Zeeuw, P. T., & Zhao, H. 1999, Nature, 402, 53
Helmi, A., Babusiaux, C., Koppelman, H. H., et al. 2018, Nature, 563, 85
Huang, Y., Schönrich, R., Liu, X. W., et al. 2018, ApJ, 864, 129
Ibata, R. A., Irwin, M. J., Lewis, G. F., Ferguson, A. M. N., & Tanvir, N. 2003, MNRAS, 340, L21
Jordi, C., Gebran, M., Carrasco, J. M., et al. 2010, A&A, 523, A48
Kaluzny, J. 1994, A&AS, 108, 151
Katz, D., Sartoretti, P., Cropper, M., et al. 2019, A&A, 622, A205
Kawata, D., Baba, J., Ciucă, I., et al. 2018, MNRAS, 479, L108
Kawata, D., Baba, J., Hunt, J. A. S., et al. 2020, MNRAS, submitted, [arXiv:2012.05890]
Kazantzidis, S., Bullock, J. S., Zentner, A. R., Kravtsov, A. V., & Moustakas, L. A. 2008, ApJ, 688, 254
Khanna, S., Sharma, S., Bland-Hawthorn, J., et al. 2019a, MNRAS, 482, 4215
Khanna, S., Sharma, S., Tepper-Garcia, T., et al. 2019b, MNRAS, 489, 4962
Koppelman, H. H., Helmi, A., Massari, D., Roelenga, S., & Bastian, U. 2019, A&A, 625, A5
Krone-Martins, A., & Moitinho, A. 2014, A&A, 561, A57
Lallement, R., Babusiaux, C., Vergely, J. L., et al. 2019, A&A, 625, A135
Laporte, C. F. P., Johnston, K. V., Gómez, F. A., Garavito-Camargo, N., & Besla, G. 2018, MNRAS, 481, 286
Laporte, C. F. P., Minchev, I., Johnston, K. V., & Gómez, F. A. 2019a, MNRAS, 485, 3134
Laporte, C. F. P., Johnston, K. V., & Tzanidakis, A. 2019b, MNRAS, 483, 1427
Laporte, C. F. P., Belokurov, V., Koposov, S. E., Smith, M. C., & Hill, V. 2020a, MNRAS, 492, L61
Laporte, C. F. P., Famaey, B., Monari, G., et al. 2020b, A&A, 643, L3
Lata, S., Pandey, A. K., Sagar, R., & Mohan, V. 2002, A&A, 388, 158
Law, D. R., & Majewski, S. R. 2010, ApJ, 714, 229
Li, J., Newberg, H. J., Carlin, J. L., et al. 2012, ApJ, 757, 151
Li, T. S., Sheffield, A. A., Johnston, K. V., et al. 2017, ApJ, 844, 74
Lindegren, L., Hernández, J., Bombrun, A., et al. 2018, A&A, 616, A2
Lindegren, L., Bastian, U., Biermann, M., et al. 2021a, A&A, 649, A4 (*Gaia* EDR3 SI)
Lindegren, L., Klioner, S. A., Hernández, J., et al. 2021b, A&A, 649, A2 (*Gaia* EDR3 SI)
López-Corredoira, M., & Molgó, J. 2014, A&A, 567, A106
López-Corredoira, M., Allende Prieto, C., Garzón, F., et al. 2018, A&A, 612, L8
López-Corredoira, M., Garzón, F., Wang, H. F., et al. 2020, A&A, 634, A66
Lucey, M., Ting, Y.-S., Ramachandra, N. S., & Hawkins, K. 2020, MNRAS, 495, 3087
Luri, X., Palmer, M., Arenou, F., et al. 2014, A&A, 566, A119
Luri, X., Brown, A. G. A., Sarro, L. M., et al. 2018, A&A, 616, A9
Lutz, T. E., & Kelker, D. H. 1973, PASP, 85, 573
Mackereth, J. T., Bovy, J., Leung, H. W., et al. 2019, MNRAS, 489, 176
Majewski, S. R., Skrutskie, M. F., Weinberg, M. D., & Ostheimer, J. C. 2003, ApJ, 599, 1082
Majewski, S. R., Ostheimer, J. C., Rocha-Pinto, H. J., et al. 2004, ApJ, 615, 738
Marasco, A., Fraternali, F., van der Hulst, J. M., & Oosterloo, T. 2017, A&A, 607, A106
Marigo, P., Girardi, L., Bressan, A., et al. 2017, ApJ, 835, 77
Martin, N. F., Ibata, R. A., Bellazzini, M., et al. 2004, MNRAS, 348, 12
Martin, N. F., Ibata, R. A., & Irwin, M. 2007, ApJ, 668, L123
Martinez-Medina, L., Pichardo, B., Peimbert, A., & Valenzuela, O. 2019, MNRAS, 485, L104
Martinez-Medina, L. A., Pichardo, B., & Peimbert, A. 2020, MNRAS, 496, 1845
Martinsson, T. P. K., Verheijen, M. A. W., Westfall, K. B., et al. 2013, A&A, 557, A130
Mateo, M., Mirabal, N., Udalski, A., et al. 1996, ApJ, 458, L13
McGaugh, S. S. 2019, ApJ, 885, 87
McMillan, P. J. 2017, MNRAS, 465, 76
McMillan, P. J. 2018, Res. Notes AAS, 2, 51
Minniti, D., Saito, R. K., Alonso-García, J., Lucas, P. W., & Hempel, M. 2011, ApJ, 733, L43
Momany, Y., Zaggia, S. R., Bonifacio, P., et al. 2004, A&A, 421, L29
Momany, Y., Zaggia, S., Gilmore, G., et al. 2006, A&A, 451, 515
Monari, G., Famaey, B., Siebert, A., Wegg, C., & Gerhard, O. 2019, A&A, 626, A41

Newberg, H. J., Yanny, B., Rockosi, C., et al. 2002, ApJ, 569, 245
Peñarrubia, J., Martínez-Delgado, D., Rix, H. W., et al. 2005, ApJ, 626, 128
Poggio, E., Drimmel, R., Lattanzi, M. G., et al. 2018, MNRAS, 481, L21
Price-Whelan, A. M., Johnston, K. V., Sheffield, A. A., Laporte, C. F. P., & Sesar, B. 2015, MNRAS, 452, 676
Purcell, C. W., Bullock, J. S., Tollerud, E. J., Rocha, M., & Chakrabarti, S. 2011, Nature, 477, 301
Ramos, P., Antoja, T., & Figueras, F. 2018, A&A, 619, A72
Ramos, P., Mateu, C., Antoja, T., et al. 2020, A&A, 638, A104
Ramos, P., Antoja, T., Mateu, C., et al. 2021, A&A, 646, A99
Reid, M. J., & Brunthaler, A. 2020, ApJ, 892, 39
Reid, M. J., Menten, K. M., Zheng, X. W., et al. 2009, ApJ, 700, 137
Riello, M., De Angeli, F., Evans, D. W., et al. 2021, A&A, 649, A3 (*Gaia* EDR3 SI)
Robin, A. C., Reylé, C., Derrière, S., & Picaud, S. 2003, A&A, 409, 523
Robin, A. C., Luri, X., Reylé, C., et al. 2012, A&A, 543, A100
Rocha-Pinto, H. J., Majewski, S. R., Skrutskie, M. F., Crane, J. D., & Patterson, R. J. 2004, ApJ, 615, 732
Rocha-Pinto, H. J., Majewski, S. R., Skrutskie, M. F., et al. 2006, ApJ, 640, L147
Romero-Gómez, M., Mateu, C., Aguilar, L., Figueras, F., & Castro-Ginard, A. 2019, A&A, 627, A150
Ruiz-Dern, L., Babusiaux, C., Arenou, F., Turon, C., & Lallement, R. 2018, A&A, 609, A116
Sancisi, R. 2004, IAU Symp, 220, 233
Sanders, J. L., & Das, P. 2018, MNRAS, 481, 4093
Schlafly, E. F., & Finkbeiner, D. P. 2011, ApJ, 737, 103
Schlegel, D. J., Finkbeiner, D. P., & Davis, M. 1998, ApJ, 500, 525
Schönrich, R., & Aumer, M. 2017, MNRAS, 472, 3979
Schönrich, R., & Dehnen, W. 2018, MNRAS, 478, 3809
Schönrich, R., Binney, J., & Dehnen, W. 2010, MNRAS, 403, 1829
Seabroke, G., Fabricius, C., Teyssier, D., et al. 2021 A&A, submitted (Gaia EDR3 SI)
Sharma, S., Hayden, M. R., Bland-Hawthorn, J., et al. 2020, MNRAS, submitted [arXiv:2004.06556]
Sheffield, A. A., Johnston, K. V., Majewski, S. R., et al. 2014, ApJ, 793, 62
Sheffield, A. A., Price-Whelan, A. M., Tzanidakis, A., et al. 2018, ApJ, 854, 47
Siebert, A., Famaey, B., Minchev, I., et al. 2011, MNRAS, 412, 2026
Skrutskie, M. F., Cutri, R. M., Stiening, R., et al. 2006, AJ, 131, 1163
Slater, C. T., Bell, E. F., Schlafly, E. F., et al. 2014, ApJ, 791, 9
Sofue, Y. 2020, Galaxies, 8, 37
Strömberg, G. 1927, ApJ, 65, 238
Tosi, M., Di Fabrizio, L., Bragaglia, A., Carusillo, P. A., & Marconi, G. 2004, MNRAS, 354, 225
Vande Putte, D., Garnier, T. P., Ferreras, I., Mignani, R. P., & Cropper, M. 2010, MNRAS, 407, 2109
van der Kruit, P. C., & Freeman, K. C. 1986, ApJ, 303, 556
Wang, Q., Wang, Y., Liu, C., Mao, S., & Long, R. J. 2017, MNRAS, 470, 2949
Wang, H., López-Corredoira, M., Carlin, J. L., & Deng, L. 2018, MNRAS, 477, 2858
Wang, H. F., López-Corredoira, M., Huang, Y., et al. 2020a, MNRAS, 491, 2104
Wang, H. F., Huang, Y., Zhang, H. W., et al. 2020b, ApJ, 902, 70
Weiland, J. L., Arendt, R. G., Berriman, G. B., et al. 1994, ApJ, 425, L81
Widrow, L. M., Gardner, S., Yanny, B., Dodelson, S., & Chen, H.-Y. 2012, ApJ, 750, L41
Williams, M. E. K., Steinmetz, M., Binney, J., et al. 2013, MNRAS, 436, 101
Wu, Z.-Y., Zhou, X., Ma, J., & Du, C.-H. 2009, MNRAS, 399, 2146
Xu, Y., Newberg, H. J., Carlin, J. L., et al. 2015, ApJ, 801, 105
Yanny, B., & Gardner, S. 2013, ApJ, 777, 91
Yanny, B., Newberg, H. J., Grebel, E. K., et al. 2003, ApJ, 588, 824
Yong, D., Carney, B. W., & Teixera de Almeida, M. L. 2005, AJ, 130, 597
York, D. G., Adelman, J., Anderson, J. E. J., et al. 2000, AJ, 120, 1579

[1] Institut de Ciències del Cosmos (ICCUB), Universitat de Barcelona (IEEC-UB), Martí i Franquès 1, 08028 Barcelona, Spain
[2] Lund Observatory, Department of Astronomy and Theoretical Physics, Lund University, Box 43, 22100 Lund, Sweden
[3] Université Côte d'Azur, Observatoire de la Côte d'Azur, CNRS, Laboratoire Lagrange, Bd de l'Observatoire, CS 34229, 06304 Nice Cedex 4, France
[4] Kapteyn Astronomical Institute, University of Groningen, Landleven 12, 9747 AD Groningen, The Netherlands
[5] Centro de Astronomía - CITEVA, Universidad de Antofagasta, Avenida Angamos 601, Antofagasta 1270300, Chile
[6] Mullard Space Science Laboratory, University College London, Holmbury St Mary, Dorking, Surrey RH5 6NT, UK
[7] Leiden Observatory, Leiden University, Niels Bohrweg 2, 2333 CA Leiden, The Netherlands
[8] INAF - Osservatorio astronomico di Padova, Vicolo Osservatorio 5, 35122 Padova, Italy
[9] European Space Agency (ESA), European Space Research and Technology Centre (ESTEC), Keplerlaan 1, 2201AZ, Noordwijk, The Netherlands
[10] Univ. Grenoble Alpes, CNRS, IPAG, 38000 Grenoble, France
[11] GEPI, Observatoire de Paris, Université PSL, CNRS, 5 Place Jules Janssen, 92190 Meudon, France
[12] Astronomisches Rechen-Institut, Zentrum für Astronomie der Universität Heidelberg, Mönchhofstr. 12-14, 69120 Heidelberg, Germany
[13] Institute of Astronomy, University of Cambridge, Madingley Road, Cambridge CB3 0HA, UK
[14] Department of Astronomy, University of Geneva, Chemin des Maillettes 51, 1290 Versoix, Switzerland
[15] Aurora Technology for European Space Agency (ESA), Camino bajo del Castillo, s/n, Urbanizacion Villafranca del Castillo, Villanueva de la Cañada, 28692 Madrid, Spain
[16] Lohrmann Observatory, Technische Universität Dresden, Mommsenstraße 13, 01062 Dresden, Germany
[17] European Space Agency (ESA), European Space Astronomy Centre (ESAC), Camino bajo del Castillo, s/n, Urbanizacion Villafranca del Castillo, Villanueva de la Cañada, 28692 Madrid, Spain
[18] CNES Centre Spatial de Toulouse, 18 avenue Edouard Belin, 31401 Toulouse Cedex 9, France
[19] Institut d'Astronomie et d'Astrophysique, Université Libre de Bruxelles CP 226, Boulevard du Triomphe, 1050 Brussels, Belgium
[20] F.R.S.-FNRS, Rue d'Egmont 5, 1000 Brussels, Belgium
[21] INAF - Osservatorio Astrofisico di Arcetri, Largo Enrico Fermi 5, 50125 Firenze, Italy
[22] Laboratoire d'astrophysique de Bordeaux, Univ. Bordeaux, CNRS, B18N, allée Geoffroy Saint-Hilaire, 33615 Pessac, France
[23] Max Planck Institute for Astronomy, Königstuhl 17, 69117 Heidelberg, Germany
[24] INAF - Osservatorio Astrofisico di Torino, Via Osservatorio 20, 10025 Pino Torinese (TO), Italy
[25] University of Turin, Department of Physics, Via Pietro Giuria 1, 10125 Torino, Italy
[26] DAPCOM for Institut de Ciències del Cosmos (ICCUB), Universitat de Barcelona (IEEC-UB), Martí i Franquès 1, 08028 Barcelona, Spain
[27] Royal Observatory of Belgium, Ringlaan 3, 1180 Brussels, Belgium
[28] ALTEC S.p.a, Corso Marche, 79,10146 Torino, Italy
[29] Department of Astronomy, University of Geneva, Chemin d'Ecogia 16, 1290 Versoix, Switzerland
[30] Sednai Sàrl, Geneva, Switzerland
[31] Gaia DPAC Project Office, ESAC, Camino bajo del Castillo, s/n, Urbanizacion Villafranca del Castillo, Villanueva de la Cañada, 28692 Madrid, Spain
[32] Telespazio Vega UK Ltd for European Space Agency (ESA), Camino bajo del Castillo, s/n, Urbanizacion Villafranca del Castillo, Villanueva de la Cañada, 28692 Madrid, Spain
[33] SYRTE, Observatoire de Paris, Université PSL, CNRS, Sorbonne Université, LNE, 61 avenue de l'Observatoire 75014 Paris, France
[34] National Observatory of Athens, I. Metaxa and Vas. Pavlou, Palaia Penteli, 15236 Athens, Greece
[35] IMCCE, Observatoire de Paris, Université PSL, CNRS, Sorbonne Université, Univ. Lille, 77 av. Denfert-Rochereau, 75014 Paris, France
[36] INAF - Osservatorio Astrofisico di Catania, Via S. Sofia 78, 95123 Catania, Italy
[37] Serco Gestión de Negocios for European Space Agency (ESA), Camino bajo del Castillo, s/n, Urbanizacion Villafranca del Castillo, Villanueva de la Cañada, 28692 Madrid, Spain
[38] INAF - Osservatorio di Astrofisica e Scienza dello Spazio di Bologna, Via Piero Gobetti 93/3, 40129 Bologna, Italy

[39] Institut d'Astrophysique et de Géophysique, Université de Liège, 19c, Allée du 6 Août, 4000 Liège, Belgium
[40] CRAAG - Centre de Recherche en Astronomie, Astrophysique et Géophysique, Route de l'Observatoire Bp 63 Bouzareah 16340 Algiers, Algeria
[41] Institute for Astronomy, University of Edinburgh, Royal Observatory, Blackford Hill, Edinburgh EH9 3HJ, UK
[42] ATG Europe for European Space Agency (ESA), Camino bajo del Castillo, s/n, Urbanizacion Villafranca del Castillo, Villanueva de la Cañada, 28692 Madrid, Spain
[43] ETSE Telecomunicación, Universidade de Vigo, Campus Lagoas-Marcosende, 36310 Vigo, Galicia, Spain
[44] Université de Strasbourg, CNRS, Observatoire astronomique de Strasbourg, UMR 7550, 11 rue de l'Université, 67000 Strasbourg, France
[45] Kavli Institute for Cosmology Cambridge, Institute of Astronomy, Madingley Road, Cambridge, CB3 0HA, USA
[46] Department of Astrophysics, Astronomy and Mechanics, National and Kapodistrian University of Athens, Panepistimiopolis, Zografos, 15783 Athens, Greece
[47] Observational Astrophysics, Division of Astronomy and Space Physics, Department of Physics and Astronomy, Uppsala University, Box 516, 751 20 Uppsala, Sweden
[48] Leibniz Institute for Astrophysics Potsdam (AIP), An der Sternwarte 16, 14482 Potsdam, Germany
[49] CENTRA, Faculdade de Ciências, Universidade de Lisboa, Edif. C8, Campo Grande, 1749-016 Lisboa, Portugal
[50] Department of Informatics, Donald Bren School of Information and Computer Sciences, University of California, 5019 Donald Bren Hall, 92697-3440 CA Irvine, USA
[51] Dipartimento di Fisica e Astronomia "Ettore Majorana", Università di Catania, Via S. Sofia 64, 95123 Catania, Italy
[52] CITIC, Department of Nautical Sciences and Marine Engineering, University of A Coruña, Campus de Elviña s/n, 15071, A Coruña, Spain
[53] INAF - Osservatorio Astronomico di Roma, Via Frascati 33, 00078 Monte Porzio Catone (Roma), Italy
[54] Space Science Data Center - ASI, Via del Politecnico SNC, 00133 Roma, Italy
[55] Department of Physics, University of Helsinki, PO Box 64, 00014 Helsinki, Finland
[56] Finnish Geospatial Research Institute FGI, Geodeetinrinne 2, 02430 Masala, Finland
[57] STFC, Rutherford Appleton Laboratory, Harwell, Didcot, OX11 0QX, UK
[58] Institut UTINAM CNRS UMR6213, Université Bourgogne Franche-Comté, OSU THETA Franche-Comté Bourgogne, Observatoire de Besançon, BP1615, 25010 Besançon Cedex, France
[59] HE Space Operations BV for European Space Agency (ESA), Keplerlaan 1, 2201AZ, Noordwijk, The Netherlands
[60] Dpto. de Inteligencia Artificial, UNED, c/ Juan del Rosal 16, 28040 Madrid, Spain
[61] Applied Physics Department, Universidade de Vigo, 36310 Vigo, Spain
[62] Thales Services for CNES Centre Spatial de Toulouse, 18 avenue Edouard Belin, 31401 Toulouse Cedex 9, France
[63] Instituut voor Sterrenkunde, KU Leuven, Celestijnenlaan 200D, 3001 Leuven, Belgium
[64] Department of Astrophysics/IMAPP, Radboud University, PO Box 9010, 6500 GL Nijmegen, The Netherlands
[65] CITIC - Department of Computer Science and Information Technologies, University of A Coruña, Campus de Elviña s/n, 15071, A Coruña, Spain
[66] Barcelona Supercomputing Center (BSC) - Centro Nacional de Supercomputación, c/ Jordi Girona 29, Ed. Nexus II, 08034 Barcelona, Spain
[67] University of Vienna, Department of Astrophysics, Türkenschanzstraße 17, A1180 Vienna, Austria
[68] European Southern Observatory, Karl-Schwarzschild-Str. 2, 85748 Garching, Germany
[69] School of Physics and Astronomy, University of Leicester, University Road, Leicester LE1 7RH, UK
[70] Center for Research and Exploration in Space Science and Technology, University of Maryland Baltimore County, 1000 Hilltop Circle, Baltimore MD, USA
[71] GSFC - Goddard Space Flight Center, Code 698, 8800 Greenbelt Rd, 20771 MD Greenbelt, USA
[72] EURIX S.r.l., Corso Vittorio Emanuele II 61, 10128, Torino, Italy
[73] Harvard-Smithsonian Center for Astrophysics, 60 Garden St., MS 15, Cambridge, MA 02138, USA
[74] HE Space Operations BV for European Space Agency (ESA), Camino bajo del Castillo, s/n, Urbanizacion Villafranca del Castillo, Villanueva de la Cañada, 28692 Madrid, Spain
[75] CAUP - Centro de Astrofisica da Universidade do Porto, Rua das Estrelas, Porto, Portugal
[76] SISSA - Scuola Internazionale Superiore di Studi Avanzati, via Bonomea 265, 34136 Trieste, Italy
[77] Telespazio for CNES Centre Spatial de Toulouse, 18 avenue Edouard Belin, 31401 Toulouse Cedex 9, France
[78] University of Turin, Department of Computer Sciences, Corso Svizzera 185, 10149 Torino, Italy
[79] Departmento de Matemática Aplicada y Ciencias de la Computación, Univ. de Cantabria, ETS Ingenieros de Caminos, Canales y Puertos, Avda. de los Castros s/n, 39005 Santander, Spain
[80] Vera C Rubin Observatory, 950 N. Cherry Avenue, Tucson, AZ 85719, USA
[81] Centre for Astrophysics Research, University of Hertfordshire, College Lane, AL10 9AB, Hatfield, UK
[82] University of Antwerp, Onderzoeksgroep Toegepaste Wiskunde, Middelheimlaan 1, 2020 Antwerp, Belgium
[83] INAF - Osservatorio Astronomico d'Abruzzo, Via Mentore Maggini, 64100 Teramo, Italy
[84] Instituto de Astronomia, Geofìsica e Ciências Atmosféricas, Universidade de São Paulo, Rua do Matão, 1226, Cidade Universitaria, 05508-900 São Paulo, SP, Brazil
[85] Mésocentre de calcul de Franche-Comté, Université de Franche-Comté, 16 route de Gray, 25030 Besançon Cedex, France
[86] SRON, Netherlands Institute for Space Research, Sorbonnelaan 2, 3584CA, Utrecht, The Netherlands
[87] RHEA for European Space Agency (ESA), Camino bajo del Castillo, s/n, Urbanizacion Villafranca del Castillo, Villanueva de la Cañada, 28692 Madrid, Spain
[88] ATOS for CNES Centre Spatial de Toulouse, 18 avenue Edouard Belin, 31401 Toulouse Cedex 9, France
[89] School of Physics and Astronomy, Tel Aviv University, Tel Aviv 6997801, Israel
[90] Astrophysics Research Centre, School of Mathematics and Physics, Queen's University Belfast, Belfast BT7 1NN, UK
[91] Centre de Données Astronomique de Strasbourg, Strasbourg, France
[92] Université Côte d'Azur, Observatoire de la Côte d'Azur, CNRS, Laboratoire Géoazur, Bd de l'Observatoire, CS 34229, 06304 Nice Cedex 4, France
[93] Max-Planck-Institut für Astrophysik, Karl-Schwarzschild-Straße 1, 85748 Garching, Germany
[94] APAVE SUDEUROPE SAS for CNES Centre Spatial de Toulouse, 18 avenue Edouard Belin, 31401 Toulouse Cedex 9, France
[95] Área de Lenguajes y Sistemas Informáticos, Universidad Pablo de Olavide, Ctra. de Utrera, km 1. 41013, Sevilla, Spain
[96] Onboard Space Systems, Luleå University of Technology, Box 848, S-981 28 Kiruna, Sweden
[97] TRUMPF Photonic Components GmbH, Lise-Meitner-Straße 13, 89081 Ulm, Germany
[98] IAC - Instituto de Astrofisica de Canarias, Via Láctea s/n, 38200 La Laguna S.C., Tenerife, Spain
[99] Department of Astrophysics, University of La Laguna, Via Láctea s/n, 38200 La Laguna S.C., Tenerife, Spain

[100] Laboratoire Univers et Particules de Montpellier, CNRS Université Montpellier, Place Eugène Bataillon, CC72, 34095 Montpellier Cedex 05, France
[101] LESIA, Observatoire de Paris, Université PSL, CNRS, Sorbonne Université, Université de Paris, 5 Place Jules Janssen, 92190 Meudon, France
[102] Villanova University, Department of Astrophysics and Planetary Science, 800 E Lancaster Avenue, Villanova PA 19085, USA
[103] Astronomical Observatory, University of Warsaw, Al. Ujazdowskie 4, 00-478 Warszawa, Poland
[104] Laboratoire d'astrophysique de Bordeaux, Univ. Bordeaux, CNRS, B18N, allée Geoffroy Saint-Hilaire, 33615 Pessac, France
[105] Université Rennes, CNRS, IPR (Institut de Physique de Rennes) - UMR 6251, 35000 Rennes, France
[106] INAF - Osservatorio Astronomico di Capodimonte, Via Moiariello 16, 80131, Napoli, Italy
[107] Niels Bohr Institute, University of Copenhagen, Juliane Maries Vej 30, 2100 Copenhagen Ø, Denmark
[108] Las Cumbres Observatory, 6740 Cortona Drive Suite 102, Goleta, CA 93117, USA
[109] Astrophysics Research Institute, Liverpool John Moores University, 146 Brownlow Hill, Liverpool L3 5RF, UK
[110] IPAC, Mail Code 100-22, California Institute of Technology, 1200 E. California Blvd., Pasadena, CA 91125, USA
[111] Jet Propulsion Laboratory, California Institute of Technology, 4800 Oak Grove Drive, M/S 169-327, Pasadena, CA 91109, USA
[112] IRAP, Université de Toulouse, CNRS, UPS, CNES, 9 Av. colonel Roche, BP 44346, 31028 Toulouse Cedex 4, France
[113] Konkoly Observatory, Research Centre for Astronomy and Earth Sciences, MTA Centre of Excellence, Konkoly Thege Miklós út 15-17, 1121 Budapest, Hungary
[114] MTA CSFK Lendület Near-Field Cosmology Research Group, Konkoly Observatory, MTA Research Centre for Astronomy and Earth Sciences, Konkoly Thege Miklós út 15-17, 1121 Budapest, Hungary
[115] ELTE Eötvös Loránd University, Institute of Physics, 1117, Pázmány Péter sétány 1A, Budapest, Hungary
[116] Ruđer Bošković Institute, Bijenička cesta 54, 10000 Zagreb, Croatia
[117] Institute of Theoretical Physics, Faculty of Mathematics and Physics, Charles University in Prague, Czech Republic
[118] INAF - Osservatorio Astronomico di Brera, Via E. Bianchi 46, 23807 Merate (LC), Italy
[119] AKKA for CNES Centre Spatial de Toulouse, 18 avenue Edouard Belin, 31401 Toulouse Cedex 9, France
[120] Departmento de Física de la Tierra y Astrofísica, Universidad Complutense de Madrid, 28040 Madrid, Spain
[121] Vitrociset Belgium for European Space Agency (ESA), Camino bajo del Castillo, s/n, Urbanizacion Villafranca del Castillo, Villanueva de la Cañada, 28692 Madrid, Spain
[122] Department of Astrophysical Sciences, 4 Ivy Lane, Princeton University, Princeton NJ 08544, USA
[123] Departamento de Astrofísica, Centro de Astrobiología (CSIC-INTA), ESA-ESAC, Camino Bajo del Castillo s/n, 28692 Villanueva de la Cañada, Madrid, Spain
[124] naXys, University of Namur, Rempart de la Vierge, 5000 Namur, Belgium
[125] EPFL - Ecole Polytechnique fédérale de Lausanne, Institute of Mathematics, Station 8 EPFL SB MATH SDS, Lausanne, Switzerland
[126] H H Wills Physics Laboratory, University of Bristol, Tyndall Avenue, Bristol BS8 1TL, UK
[127] Sorbonne Université, CNRS, UMR7095, Institut d'Astrophysique de Paris, 98bis bd. Arago, 75014 Paris, France
[128] Porter School of the Environment and Earth Sciences, Tel Aviv University, Tel Aviv 6997801, Israel
[129] Laboratoire Univers et Particules de Montpellier, Université Montpellier, Place Eugène Bataillon, CC72, 34095 Montpellier Cedex 05, France
[130] Faculty of Mathematics and Physics, University of Ljubljana, Jadranska ulica 19, 1000 Ljubljana, Slovenia

Appendix A: Queries to the *Gaia* Archive

In this appendix we show a few examples of queries to the *Gaia* Archive[10] to retrieve the data:

Listing 1. An example of query to retrieve stars in the rectangular sky patch of the AC20 sample.

```
SELECT * from gaiaedr3.gaia_source WHERE l<190 and
    l>170 and b>-10 and b<10 }
```

Listing 2. An example of query to retrieve the number of stars and average quantities in all healpix of level 8 inside a rectangular patch in the sky.

```
SELECT sub.healpix_8,COUNT(*) as
    N,AVG(phot_g_mean_mag) as avg_g,
    AVG(visibility_periods_used) as avg_vp FROM
    (SELECT gaia_healpix_index(8, source_id) AS
    healpix_8,phot_g_mean_mag,visibility_periods_used
    FROM user_edr3int4.gaia_source WHERE l<240 AND
    l>120 AND b<60 and b>-60 AND ruwe < 1.4) AS sub
    GROUP BY sub.healpix_8
```

Appendix B: Selection of red clump stars

In this appendix we describe the selection of the RC sub-sample. First, in order to compute the absolute magnitude, we need good estimates of the extinction A_λ in band λ. For each star, one could in principle use the 2D (l, b) maps of reddening, $E(B-V)$, from Schlegel et al. (1998) which estimates the extinction at infinity. However, these 2D extinction values will overestimate the reddening. Since, we have parallax information for our sample, we can use this as a prior for distance and estimate the 3D extinction. For this, we made use of the 3D dust-reddening maps from Bayestar (Green et al. 2019). These are derived using a Bayesian scheme that combines *Gaia* parallaxes with photometry from the 2MASS and Pan-STARRS surveys, and covers the sky north of declination of $-30°$. Only 3 stars in our AC20 sample are missing from Bayestar. The multiplicative factor (f_λ) between reddening and extinction that we use is listed in Table B.1 for various bands.

For the RC selection, we first apply the following photometric cuts:

$$BP - G > 0.6, BP - RP_0 > 0.91. \tag{B.1}$$

Then, for each star, we compute the absolute magnitude (M_λ) in each of the 2MASS bands, and in *Gaia G*:

$$M_\lambda = m_\lambda - A_\lambda - \mathrm{dmod}, \tag{B.2}$$

using $\mathrm{dmod} = 5\log_{10}(100/\varpi'[\mathrm{mas}])$. Here, ϖ' is the parallax corrected for the offset of -17 μas. In Table B.1 we list the literature absolute magnitude $(\bar{M}_\lambda)$ and dispersion in various photometric bands for the RC population. Using this, for each star we can write down a likelihood function per bandpass i, and take their product

$$P_{\mathrm{RC}}(m_\lambda, A_\lambda, \varpi) = \prod_i \sqrt{2\pi}\sigma_{\bar{M}_\lambda}\mathcal{N}(M_\lambda||\bar{M}_\lambda, \sigma^*_{M_\lambda}), \tag{B.3}$$

[10] https://gea.esac.esa.int/archive/

Table B.1. Median absolute magnitude $\bar{M}_\lambda$, and dispersion in absolute magnitude $\sigma_{\bar{M}_\lambda}$ for RC stars selected from Hawkins et al. (2017).

Passband (λ)	$\bar{M}_\lambda$	$\sigma_{\bar{M}_\lambda}$	$f_\lambda = \frac{A_\lambda}{E(B-V)}$
J	-0.93 ± 0.01	0.20 ± 0.02	0.7927
H	-1.46 ± 0.01	0.17 ± 0.02	0.469
K	-1.61 ± 0.01	0.17 ± 0.02	0.3026
G	$+0.44 \pm 0.01$	0.20 ± 0.02	2.74
G_{BP}	–	–	3.374
G_{RP}	–	–	2.035

Notes. Also listed are the extinction factors (f_λ) for the four passbands used, with the 2MASS values taken from Green et al. (2019) and *Gaia* from Casagrande & VandenBerg (2018).

Table B.2. Parameters used for selecting the *RC* population.

ML	N_{RC}	$P_{\mathrm{RC}} >$	band(s)
3	121857	0.01	2MASS *J*, *Gaia G*

Notes. ML is essentially the confidence level used to set a minimum probability threshold ($P_{\mathrm{RC}} >$). Finally, N_{RC} gives the resulting number of stars classed as RC that lie between $170° < l < 190°$ and $|b| < 10°$.

where $\sigma^*_{M_\lambda} = \sqrt{\sigma^2_{\mathrm{er},M_\lambda} + \sigma^2_{\bar{M}_\lambda}}$ combines the propagated error in the absolute magnitude from Eq. (B.2), $\sigma_{\mathrm{er},M_\lambda}$, and the dispersion in the true absolute magnitude, $\sigma_{\bar{M}_\lambda}$.

For any distribution, the distance between the centroid (x_0) and a point of interest (x_1) can be given in terms of its Mahalanobis distance (ML)

$$\mathrm{ML}^2 = (x_1 - x_0)^T \Sigma^{-1} (x_1 - x_0), \tag{B.4}$$

that respects the combined covariance of x_0 and x_1, which we have written as Σ. Essentially, ML is a measure of the distance from the centroid in units of the standard deviation. Then, we can define a p-value, that is the probability of finding a value of ML^2 or more extreme under the null-hypothesis of the star not being part of the RC, from a chi-square distribution, and select those stars for which the probability (P_{RC}) is greater than the p-value:

$$P_{\mathrm{RC}} > 1 - P[\chi^2 \leq \mathrm{ML}^2]. \tag{B.5}$$

In this work we limited our analysis to a maximum of two bands, namely, *Gaia G* and 2MASS *K*. So, we used a chi-square distribution with 2 degrees of freedom, and ML is essentially the confidence level used to set a minimum probability threshold. The tolerance parameters used in our selection is shown in Table B.2, and we obtain a high quality RC sample of $N_{\mathrm{RC}} = 121857$. The HR diagram with our RC selection is shown in Fig. B.1. The parallax quality for the selection is shown in Fig. B.2, with the tail of the distribution extending down to $\sigma_\varpi/\varpi \approx 0.8$.

In Fig. C.5, we further inspect the RC selection. Panels a and b show the absolute magnitude distribution in G and K bands. We find that the median absolute magnitudes for our sample is offset from their literature values by -0.05 (G) and 0.05 (K) in the two bands. The yellow curves use the Bayestar reddening, but we also show the distribution for absolute magnitudes computed with $A_\lambda = 0$, just to illustrate that our extinction correction shifts the distribution in the correct direction. In panels c and

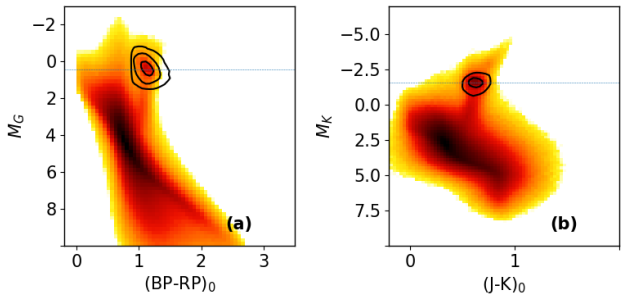

Fig. B.1. HR diagrams for the AC20 sample, with contours marking the RC selection.

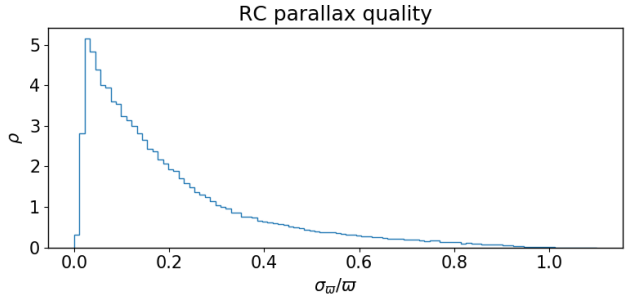

Fig. B.2. Parallax error quality of the RC sample. The tail of the distribution extends down to $\sigma_\varpi/\varpi \approx 0.8$.

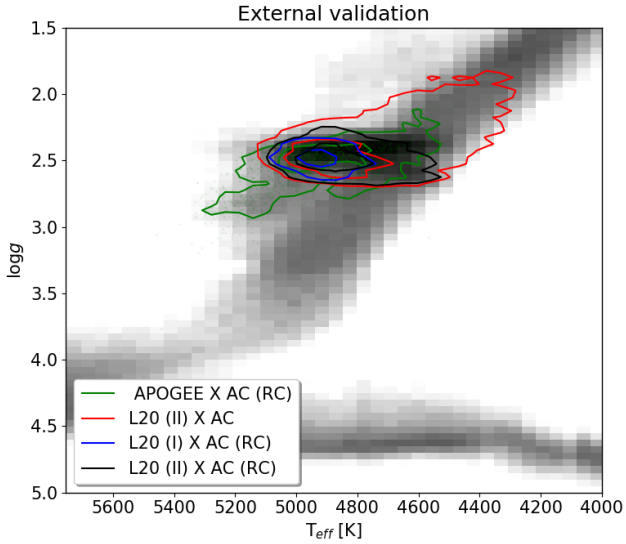

Fig. B.3. External validation comparing the distribution of the AC20 RC stars on a l Kiel diagram. In grey is the full distribution from APOGEE-DR16, and the green contours show common stars between our RC sample and APOGEE-DR16. Red contours show common stars between L20 and the entire anticentre sample used here. The blue contours show common stars between L20-'Tier I' (i.e. 20% contamination) and our RC sample. The black contours show common stars between L20-'Tier II' (i.e. 33% contamination) and our RC sample.

d, we compare the distances computed as in Appendix C.2.1, against inverse parallax. It is encouraging to see that the running median for nearby stars lies on the 1:1 line. This is further shown in panels e and f, where we look at the relative difference between the two distance estimates. Compared to inverse parallax method, our distances are slightly under (over) estimated in G (K) beyond 5 kpc from the Sun. This is likely due to the fact that distance modulus $\propto$ -M_λ. Since the literature absolute magnitudes are slightly offset, this would result in smaller distances, but the effect is minor given the small offset, especially in the K band. Finally, in panels g and h, is shown the distance error as a function of distance. The errors in the inverse parallax distances are quadratic with d, while the trend is linear for the RC distances. Beyond, $d > 5$ kpc, the errors in inverse parallax grow significantly, while for RC distances, the prediction is σ_d 1.5 kpc at 10 kpc. The distribution in Galactocentric cylindrical radius R is shown in Fig. 7. Our sample extends out to $R \sim$17 kpc, consisting of about 1000 stars at that distance.

Lucey et al. (2020) recently put out a catalogue of 2.6 million RC stars. Their method involves predicting asteroseismic parameters ($\Delta P, \Delta\nu$) and stellar parameters ($\log g, T_{\rm eff}$) from spectral energy distributions (SED). They combined photometry from Pan-STARRS, WISE, 2MASS and *Gaia*. In their catalogue (hereafter L20) they classified RC stars with contamination rate of ≈33% as 'Tier II', and a superior subset with contamination rate of ≈20% as 'Tier I'. In Fig. B.3 we show the distribution of our sample on a *Kiel* diagram by cross-matching with the L20 catalogue. We notice that their 'Tier I' sample does not have too many cooler stars. Conversely, their less stringent 'Tier II' sample, extends out to $\log g \approx$ 1.8, which is typically the lower limit of the RC range, and thus prone to contamination from regular giants.

Finally, we used APOGEE-DR16 (Ahumada et al. 2020), to construct the background Kiel diagram. This shows that our RC sample is largely concentrated around the horizontal branch (blue contour), thus missing several common stars with L20, but at the same time is likely a 'purer' sample for the purpose of distance estimation.

Appendix C: Distances to stars

C.1. Distance estimates

As discussed in Sect. 3.2 there is no existing perfect recipe for estimating distances from a measured parallax. In this work we approach this problem by testing how robust our conclusions are to the use of different distance estimators. We used three different methods, which we tested with the mock *Gaia* data from GOG (described in Sect. 2.2):

1. d_ϖ: simple inversion of parallax $1/\varpi$.

2. d_{PM}: Bayesian distances with an iterative prior. This approach is closely related to that used by Schönrich & Aumer (2017). In general, the Bayesian approach relies on the statement that for an observed parallax, ϖ, and uncertainty, σ_ϖ, the probability of a given distance d is

$$P(d|\varpi, \sigma_\varpi) \propto P(\varpi|d, \sigma_\varpi)\, P(d),$$

where $P(d)$ is the prior on distance. This prior takes three factors into account. Firstly, the volume at distances between d and $d + \delta d$ increases like d^2. Secondly, the true spatial distribution of stars is not uniform. Thirdly, there are selection effects: the probability of a star at distance d entering the catalogue varies with d because there is a magnitude limit to the survey (because for example intrinsically faint stars become too faint to enter the catalogue).

For the distances $d_{\rm PM}$, these considerations lead us to a prior $P(d) \propto d^2 P(r(d)) S(d)$, where $S(d)$ is the selection function, and $r(d)$ is the position in a galaxy of an object at distance d along

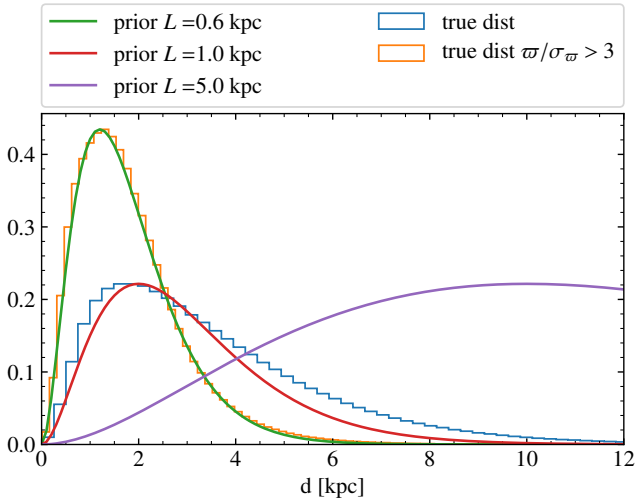

Fig. C.1. Distribution of true distances of GOG in the anticentre. We show all stars in GOG (blue histogram) and stars with $\varpi/\sigma_\varpi > 3$ (orange histogram). The different solid lines are the exponential decreasing prior (Eq. (C.1)) with scalelength of 0.6, 1 and 5 kpc.

a given line-of-sight, so $P(r(d))$ is proportional to the density of a model Galaxy. The distance estimate, $\tilde{d}$ and uncertainty σ_d is then found as the expectation value and standard deviation of d given this prior and the measured parallax (with uncertainty).

The model from which we take $P(r(d))$ is taken from McMillan (2018), and has two exponential discs (thin and thick) and a power-law halo. It has no warp. We approximated the selection function as $S(d) \propto \exp(-d/L_s)$ where L_s is a value we determine. Experiments with GOG (see below) and investigation with the *Gaia* data both suggest that this is a reasonable approximation.

Following Schönrich & Aumer (2017), we derived the selection function from the data by recognising that $S(d) \propto N(d)/(d^2 \int \rho(d,l,b) \cos b dl\, db)$ where $N(d)$ is the number of stars in the catalogue at a distance d and the integral over ℓ, b is taken over the field we consider. We don't know $N(d)$, but we can make the approximation that $N(d) \approx N(\tilde{d})$ for some range of distances and subset of the more accurate parallaxes. We used this to find the scale length L_s which enters into $S(d)$. We then iterated this process – using this estimate of the selection function to find new distance estimates, $\tilde{d}$, then using these to make a new estimate of $S(d)$. Experiments with GOG indicate that fitting $S(d)$ for distances $1 < d/\mathrm{kpc} < 3$ and for stars with $\varpi/\sigma_\varpi > 3$ give a reasonable approximation. The value of L_s we find converges after a few iterations and we find $L_s = 0.963$ for our sample and $L_s = 1.16$ for GOG.

3. d_L: Bayesian distances with exponentially decreasing prior with scale length of L following Bailer-Jones et al. (2018). These distances were computed following Bailer-Jones et al. (2018) with a simpler prior, in particular an exponentially decreasing prior with distance d:

$$P(d|L), = \begin{cases} \frac{1}{2L^3} d^2 e^{-d/L} & \text{if } d > 0 \\ 0 & \text{otherwise.} \end{cases} \quad \text{(C.1)}$$

Figure C.1 shows the true distribution of distances of GOG (blue histogram) and the same for a selection of sources with $\varpi/\sigma_\varpi > 3$ (orange histogram). As explained in Bailer-Jones et al. (2018), a good approximation for the maximum likelihood

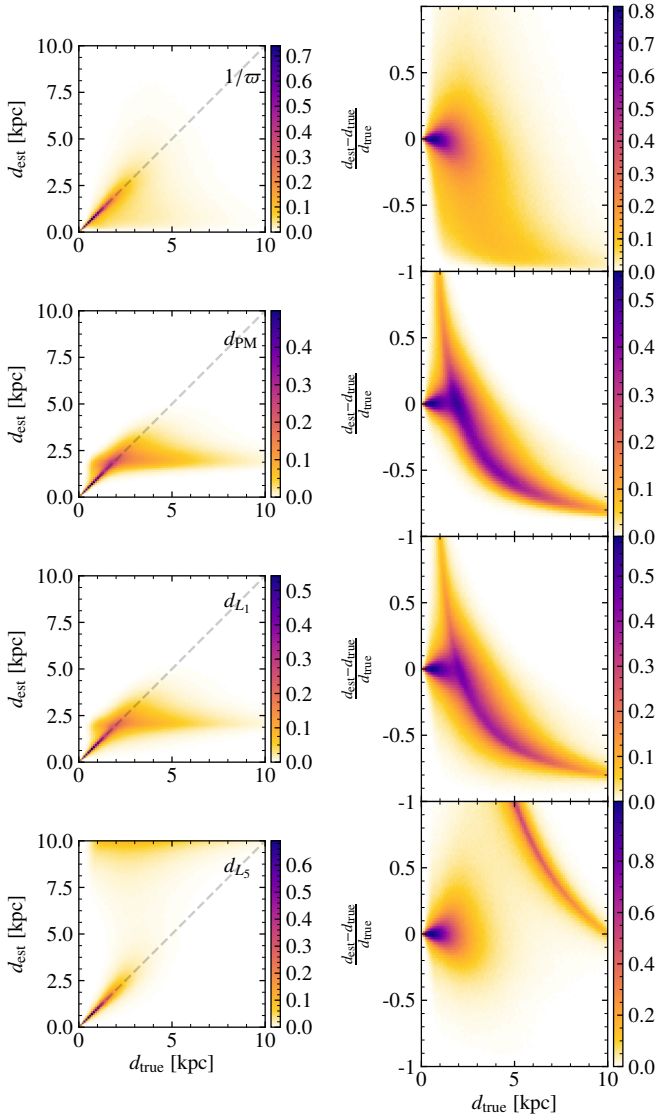

Fig. C.2. True versus estimated distances for different methods. *Left*: direct comparison between true and estimated distances of GOG for the different distance estimations as indicated in the legends. *Right*: fractional error in the estimated distance as a function of true distance for the same estimators.

estimate for the scale-length L of the prior Eq. (C.1) of a given distance distribution is MED(d)/3, where MED(d) is the median of the distribution. For GOG in the anticentre this turns out to be 0.977 kpc and 0.527 kpc for stars with $\varpi/\sigma_\varpi > 3$. The red and green solid lines show the shape of the prior with $L = 1$ kpc and $L = 0.6$ kpc, respectively, which fairly reproduce the true distribution of distances in each case. We also show the prior for $L = 5$ kpc. Hereafter, we choose two different scale-length L of 1 kpc (that we name d_{L_1}) and 5 kpc (d_{L_5}), motivated by the tests shown below. While Bailer-Jones et al. (2018) uses a scale-length that depends on the sky coordinates, here for simplicity we use a single value for the whole field of 20×20 deg.

C.2. Tests with GOG

Here we test the different distances estimations with GOG. First we note that due to deficiencies in the *Gaia* error model,

the uncertainties in the astrometric values in GOG somewhat disagree with the values for EDR3. In particular, we see an overestimation of the parallax errors as a function of magnitude G, actually more similar to the DR2 scenario than to EDR3 (Fig. E.1 top). The exercises presented here thus show a worse case scenario.

Figure C.2 shows the comparison between true distance and estimated distance for the different methods presented above applied to the whole GOG sample, for which the true distances are known. We see in the left panels a good fraction of stars with properly determined distances falling on the 1:1 line (those with small parallax uncertainties). However, we also see large fraction of stars with badly estimated distances corresponding to parallaxes with large uncertainty (including negative parallaxes). For the d_ϖ case (top panels), most of these problematic cases appear scattered in the underestimated region. For Bayesian estimations $d_{\rm PM}$, d_{L_1} and d_{L_5} (three bottom panels), they appear concentrated at the nearly horizontal line at $d_{\rm est} = 2L$ (coinciding with two times the mode of the prior, that is ∼2 kpc in the two middle rows, and 10 kpc for the bottom row), completely dominated by the choice of the prior as explained in Bailer-Jones et al. (2018). These numerous uninformative parallaxes forces us to perform a cut in fractional parallax uncertainty, which, unfortunately, may introduce biases in our samples as discussed for instance in Luri et al. (2018).

Figure C.3 shows the fractional error in the estimated distance as a function of fractional error in parallax with different panels for different distance estimations. All panels show large errors for large parallax uncertainties (smaller ϖ/σ_ϖ) as expected and highlight the need to use a certain criteria to select good parallaxes while finding a proper balance with the final number of sources kept and trying not to bias the sample as a result of eliminating specific populations. Depending on the particular analysis, these considerations might lead to different choices. Here we choose to select sources with $\varpi/\sigma_\varpi > 3$ in the case of the AC20 sample (dash-dotted vertical line) while a more restrictive cut at $\varpi/\sigma_\varpi > 5$ is used in Sect. 5.1 (dotted line).

From Fig. C.3 we also note two important aspects. First, the performance of the 4 different methods is quite similar when one chooses cuts in ϖ/σ_ϖ as the ones mentioned above, with only a slight underestimation of the distances in the case of d_ϖ compared for instance to $d_{\rm PM}$. Second, we also want to emphasise that, even if the median differences between estimated and true distances are small, at $\varpi/\sigma_\varpi > 5$ (dotted vertical line) 50% of the sources have errors in the derived distances $\gtrapprox$20% (sources outside the shaded areas which enclose the other 50%) independently of the method used.

Now focusing on the selection of sources with $\varpi/\sigma_\varpi > 3$, the distance error of these different estimators as a function of true distances is shown in Fig. C.4. We see a slightly better performance of the d_{L_5} at larger distances but a better one for d_{L_1} at nearby distances. The d_ϖ is underestimated in median for all distances while $d_{\rm PM}$ shows overestimated distances at nearby distances, but the contrary beyond 2 kpc. Apart from these little differences, we note that non of the estimators is completely free of bias even with the selection of $\varpi/\sigma_\varpi > 3$, as already mentioned above. We see underestimations of the distance that start to be important (20%) at around 4 kpc and biases larger than ∼40% for 25% of the sources at this same distance. Again we emphasise that the parallax errors in GOG are overestimated with respect to *Gaia* EDR3, and therefore the expected biases as a function of distance in EDR3 are possibly smaller than shown here.

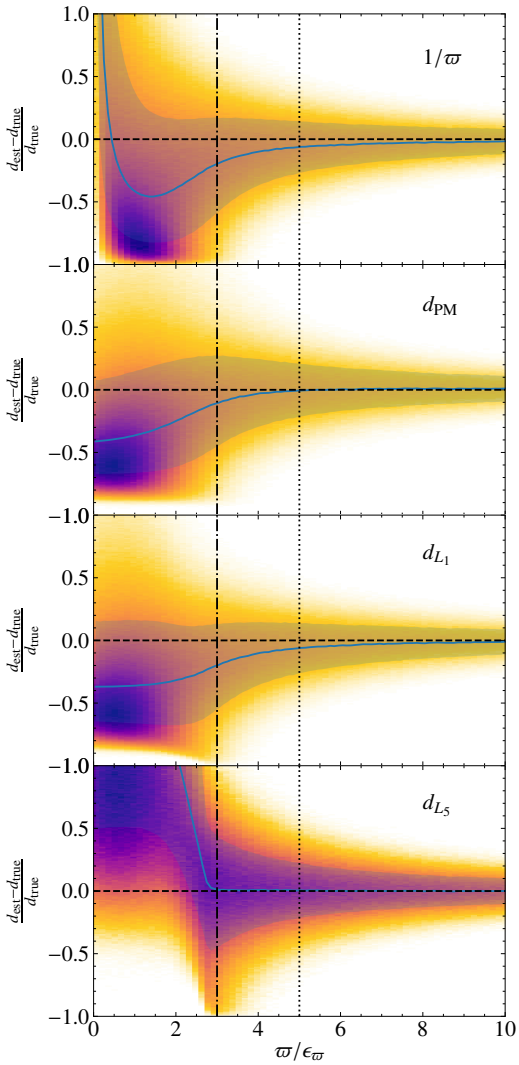

Fig. C.3. Fractional error in the estimated distance as a function of fractional error in parallax. We show the errors for the different distance estimations as indicated in the labels for the GOG sample. Solid lines indicate the median fractional error and shaded areas show the 25 and 75% quartiles.

All these tests show that different priors might work better in different regimes and that there can be multiple criteria to choose which method provides a better estimate (e.g. minimising the median distance error at small versus large distances). We also need to keep in mind that these conclusions are somewhat model dependent, influenced by the particular MW density model and selection function imposed in GOG. Our approach of exploring varied distances estimations wants to mitigate this model-dependency and the appropriateness of different methods and priors in different cases. We highlight that it is necessary to evaluate the impact of these biases and the effects of the parallax quality cut on the different analysis.

So far what we showed regarded only the estimation of the distance. This estimation and a single value for its uncertainty is then used, together with the proper motions, to calculate velocities and their uncertainties. However, we know this is not strictly correct. On one hand, because the proper motion errors are correlated with the parallax errors and, on the other, because the

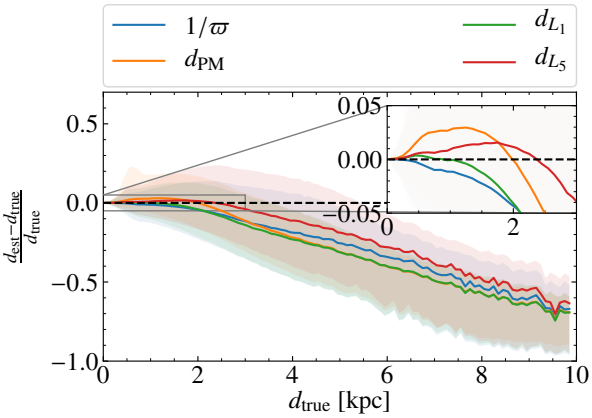

Fig. C.4. Median fractional error in the estimated distance for good quality parallaxes. We show the errors as a function of true distance for different distance estimations as indicated in the labels for stars with $\varpi/\sigma_\varpi > 3$ in the GOG sample. Solid lines indicate the median fractional error and shaded areas show the 25 and 75% quartiles.

distribution of uncertainties in the estimated distance in general is not Gaussian and asymmetric. Ideally, then, one would use a method to estimate simultaneously the distance and the tangential velocity of each star. The *Gaia* technical note GAIA-C8-TN-MPIA-CBJ-081 described a way to infer velocities and distances at the same time, from the proper motions and parallax, using a Markov chain Monte Carlo (MCMC) method. This approach is mathematically more accurate and allows us to deal properly with the correlations between velocities and distances. We have tested it with a random subset of the GOG sample and conclude, firstly, that the resulting velocities are similar to the ones obtained with the usual and simpler approach; secondly, that the correlation between velocities and distances is dominated by the transformation rather than by the correlation in the uncertainties; thirdly, that a cut in parallax quality is still necessary; and, finally, that the high computation cost renders it unfeasible to use for even modest-sized samples. For all these reasons, we do not use it here.

C.2.1. Red clump distances

For each star classified as RC, we can invert Eq. (B.2) to calculate the distance modulus. For this we used the literature absolute magnitudes in each band pass, $\bar{M}_\lambda$. The errors in the computed distances using the RC and parallax only is given by,

$$\sigma_{d_{RC,\lambda}} = 0.2\ln(10)\sigma_{M_\lambda} d \tag{C.2}$$

$$\sigma_{d_\varpi} = \sigma_\varpi d^2, \tag{C.3}$$

where σ_{M_λ} is the dispersion in the computed absolute magnitudes of the RC selection, and σ_ϖ is the parallax error. The parameters in Table B.2 are fine tuned in order to maximise the number of RC stars and minimise the dispersion and thus the errors in distances.

As mentioned earlier, we did not apply the 'qfl' quality flag on 2MASS photometry, but instead use the photometric errors to decide if the distances will be estimated using the K band or G band. In general, the K band suffers from lower extinction than the broader G band, so we prefer to use distances estimated using

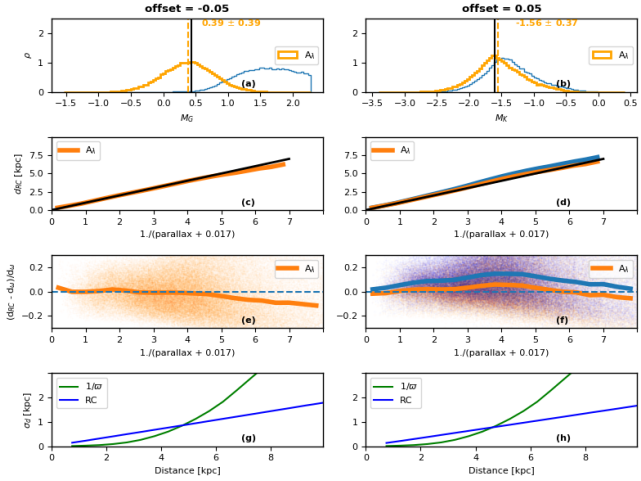

Fig. C.5. Red clump sample inspection. (*a* and *b*) Absolute magnitudes in G and K for the selected sample. The yellow curves use the 3D extinctions from Bayestar, while the blue curves are for zero extinction shown just for illustration of shift towards the correct literature value upon reddening correction. *Panels c–f* compare the RC distances to inverse parallax, while *panels g and h* show the error in distances as a function of d for the two methods. Beyond 5 kpc, RC distances become more reliable than inverse parallax.

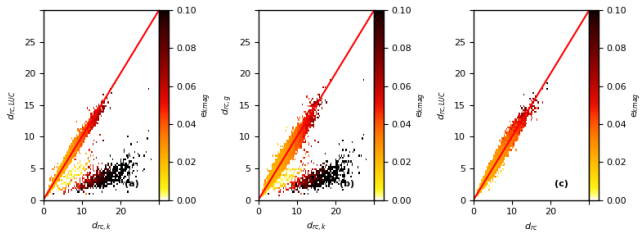

Fig. C.6. Red clump distance validation with the external catalogue L20. To enhance the illustration we use a larger RC sample here ($147° < l < 219°$ and $|b| < 30°$). *Panel a*: comparison to L20 shows the presence of a population for which distances are overestimated using the K band. This is due to very high photometric errors (i.e. (*e_jmag*| *e_kmag*) > 0.025). (*b*) Comparison between G and K band derived distances also highlights the same trend: K band distances are overestimated for poor photometry stars. (*c*) Replacing K band estimates with G where (*e_jmag*| *e_kmag*) > 0.025 improves agreement with L20.

K. However, if for a given star the photometric errors, (*e_jmag*| *e_kmag*) > 0.025, the typical value above which photometry in 2MASS becomes unreliable, then we estimate distances for these using the G band. This is illustrated in Fig. C.6, where we compare our distance estimates to the external catalogue of L20. Essentially, for stars with poor 2MASS photometry we overestimate the distances if the K band is used. Replacing these with G band estimates results in a much better agreement with the external catalogue.

C.2.2. Comparison of the different distances for EDR3

Finally, Fig. C.7 compares all sets of distances derived in this work using the $d_{\rm PM}$ case as a baseline (see caption for more details).

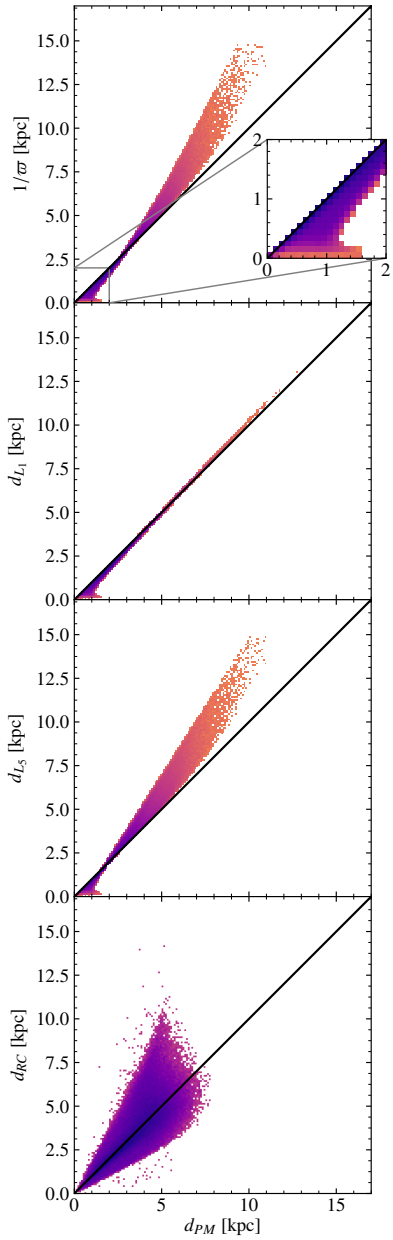

Fig. C.7. Comparison of the different distances used in this study. The comparison is done with respect to the $d_{\rm PM}$ distances. The discrepancies are small for small distances. For the case of the RC, we only compare stars with $\varpi/\sigma_\varpi > 3$, since the rest of RC sources are not included in our set of $d_{\rm PM}$. This is then misleading since for these stars the parallax retrieves better distances, but the real gain for the RC occurs exactly for the stars missing in this panel, in the regime where the photometric distances might be better than the ones from parallax alone. The peculiar shape shown in the inset of the *top panel* and present in the *three top panels* is composed of stars with large parallax error, for which the expectation values used in the $d_{\rm PM}$ estimation are larger than for instance the medians used in d_L.

Appendix D: Parallax zero point

In this appendix we illustrate the differences in distance and velocities when different parallax zero points are used (Fig. D.1), and we reproduce several figures of the main part done with and without different parallax zero points (Figs. D.2 and D.3).

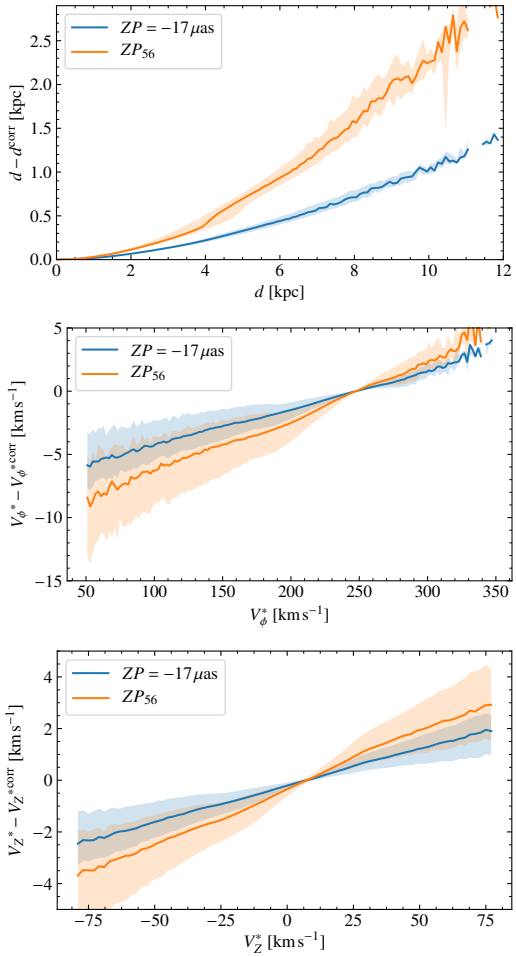

Fig. D.1. Effects of the zero point in parallax on distances and velocities. The comparison is done with respect to the case with the Bayesian distances $d_{\rm PM}$ where the zero point is not considered (x axis) and the shaded areas show the percentiles 10 and 90 (i.e. they enclose 80% of stars). *Top panel*: we see how not correcting for the zero point produces overestimated distances. The zero point prescription $\rm ZP_{56}$ reduces even more the distances compared to the case of a fixed zero point $\rm ZP = -17\,\mu as$. The velocities (*middle and bottom*) scale linearly with the distance and thus we see the absolute magnitude of the velocities being larger when the zero point is not considered. We see null differences in the case of null proper motion, that is when the velocities equal that of the Local Standard of Rest.

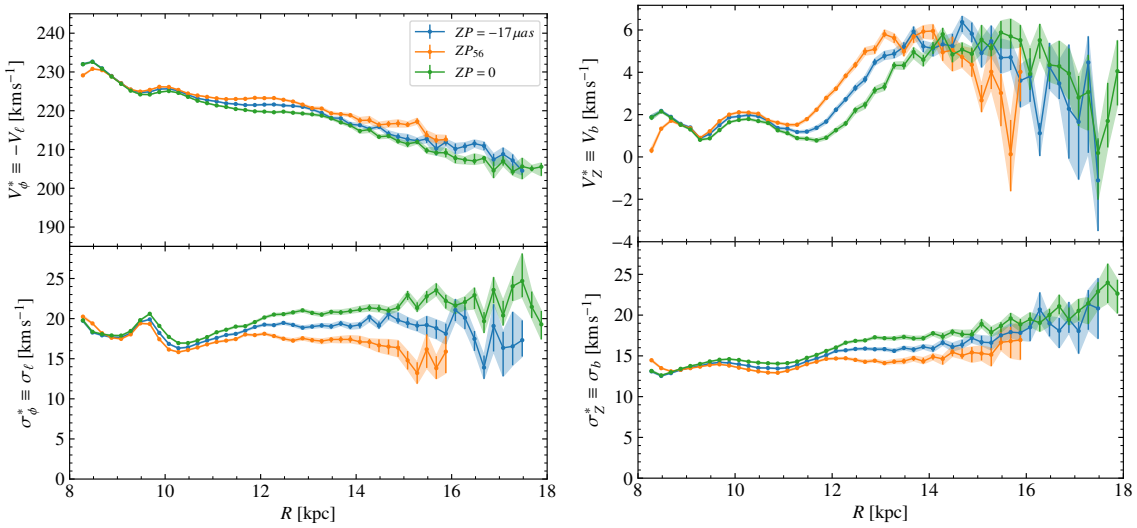

Fig. D.2. Velocity profiles for different parallax zero points. In the rotation curve (*top left*), as expected, the rotation curve computed using ZP_{56} (orange curve) is slightly shifted to the left (R decreases by about 0.5 kpc at $R = 14$ kpc) and V^*_ϕ also decreases, but always in amounts smaller than $\sim 2\,\mathrm{km\,s^{-1}}$. In the vertical velocity plot (*top right*), we observe similar effects, though a notable effect is seen in the first kpc. The velocity dispersions (computed as the *mad* values, *bottom*) appear also slightly different, with ZP_{56} yielding smaller dispersions but without changing the overall shape.

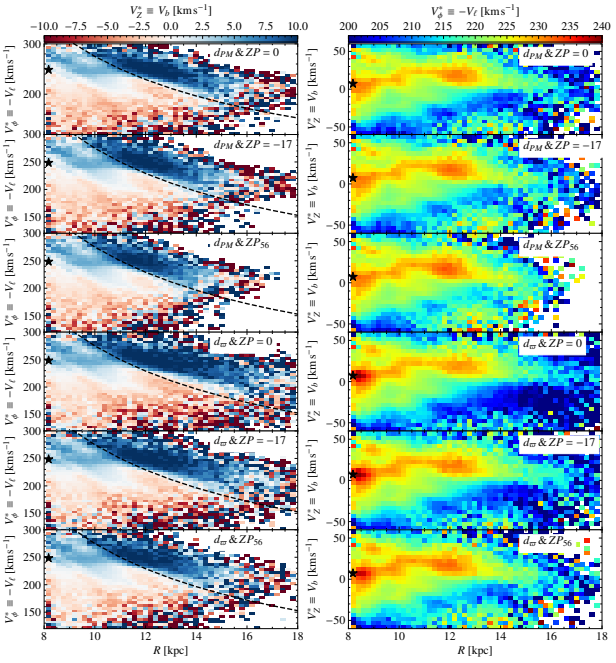

Fig. D.3. Phase space projections for different parallax zero point. The plot reproduces panels b and e of Fig. 14 using different distance estimations and parallax zero point as indicated in the legends. As explained in other parts of the article, the correction of the zero point combined with the different distance estimators used produce a change in the distance scale but in any case induces or removes the phase space substructure such as the one observed in this panels. The smallest distances are found when the Bayesian distances d_{PM} and the zero point ZP_{56} are used.

Appendix E: Additional material

In this appendix we present a miscellanies set of plots that serve as supporting material to the rest of the sections. A describing text can be found in each of the figures.

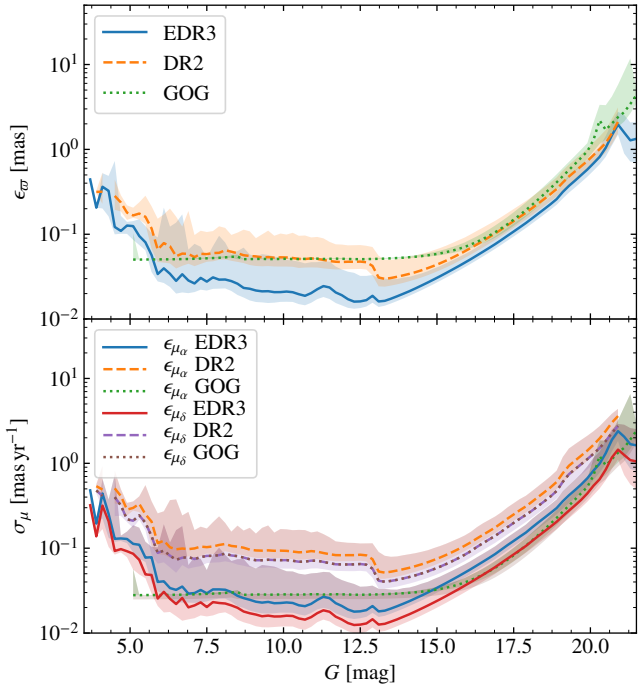

Fig. E.1. Comparison of the astrometric uncertainties for DR2, EDR3 and GOG. Due to deficiencies in the GOG *Gaia* error model, the astrometric uncertainties in GOG do not match perfectly those for EDR3. The error model retrieves unique values of the formal uncertainties as a function of G, while a large range is obtained for the data (shaded areas showing the 10 and 90% percentiles). We also see an overestimation of the parallax errors (*top*), which actually look more similar to the DR2 scenario than to EDR3. By definition, the errors in μ^*_α and μ_δ are the same for GOG. The errors of the proper motions are closer to the true uncertainties although no distinction between the different components is made for this mock data.

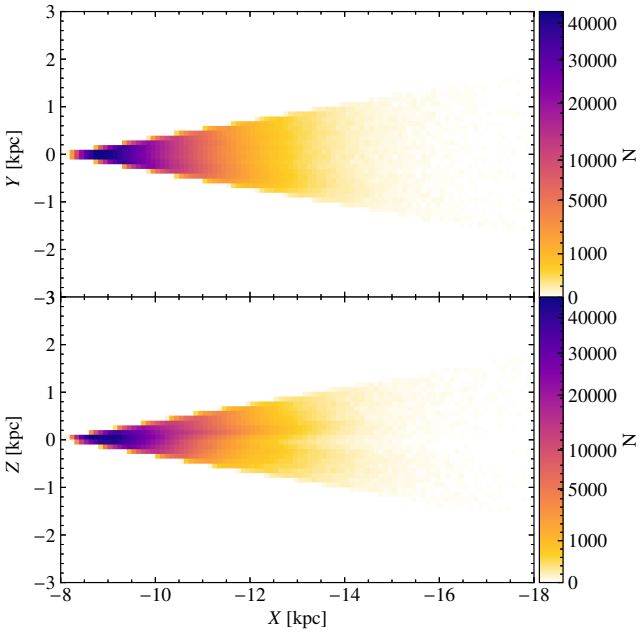

Fig. E.2. Spatial distribution of the AC20-$\varpi/\sigma_\varpi > 3$. (*a*) Counts in bins of 0.1 kpc in the *X*-*Y* projection. (*b*) Same but for the *X*-*Z* projection.

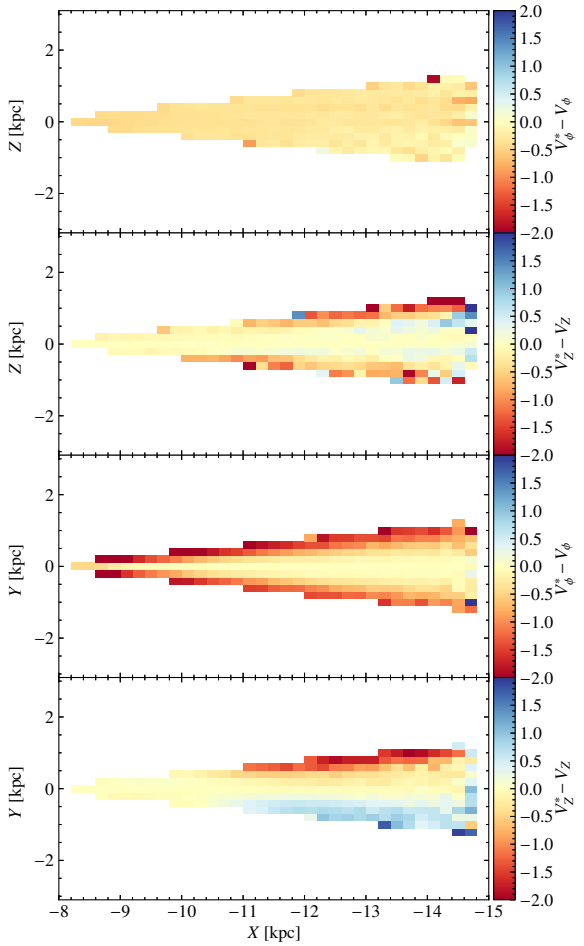

Fig. E.3. Error in the velocities for GOG when using our approximations. Median differences between V_ϕ^* and V_ϕ, and between V_Z^* and V_Z (Eqs. (4) and (5)) in bins in the *X*-*Y* and *X*-*Z* projections.

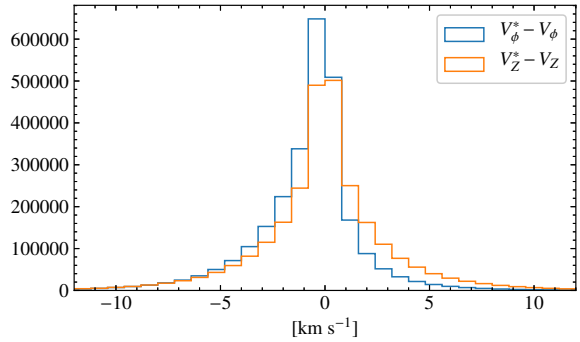

Fig. E.4. Error in the velocities for GOG when using our approximations (part 2). The histogram of the differences between V_ϕ^* and V_ϕ, and between V_Z^* and V_Z is shown. The 10 and 90% percentiles of the differences are -1.5 and 3.9 km s^{-1} and -3.6 and 3.4 for $V_\phi*$ and for V_Z*, respectively.

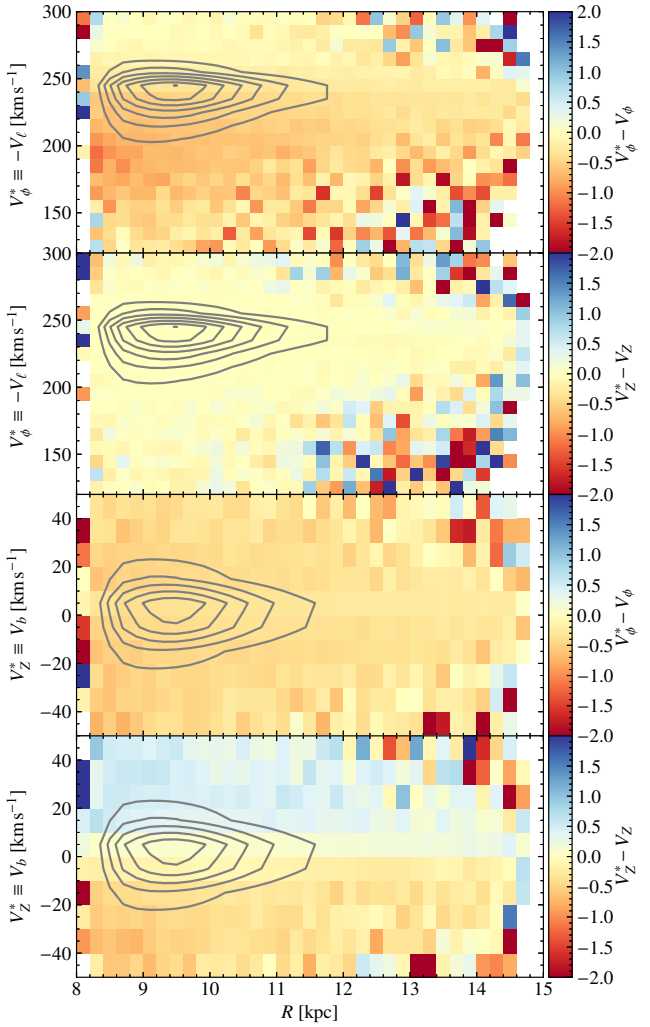

Fig. E.5. Error in the velocities for GOG when using our approximations (part 3). Median differences between V_ϕ^* and V_ϕ, and between V_Z^* and V_Z in bins in the R-V_ϕ^* and R-V_Z^* projections.

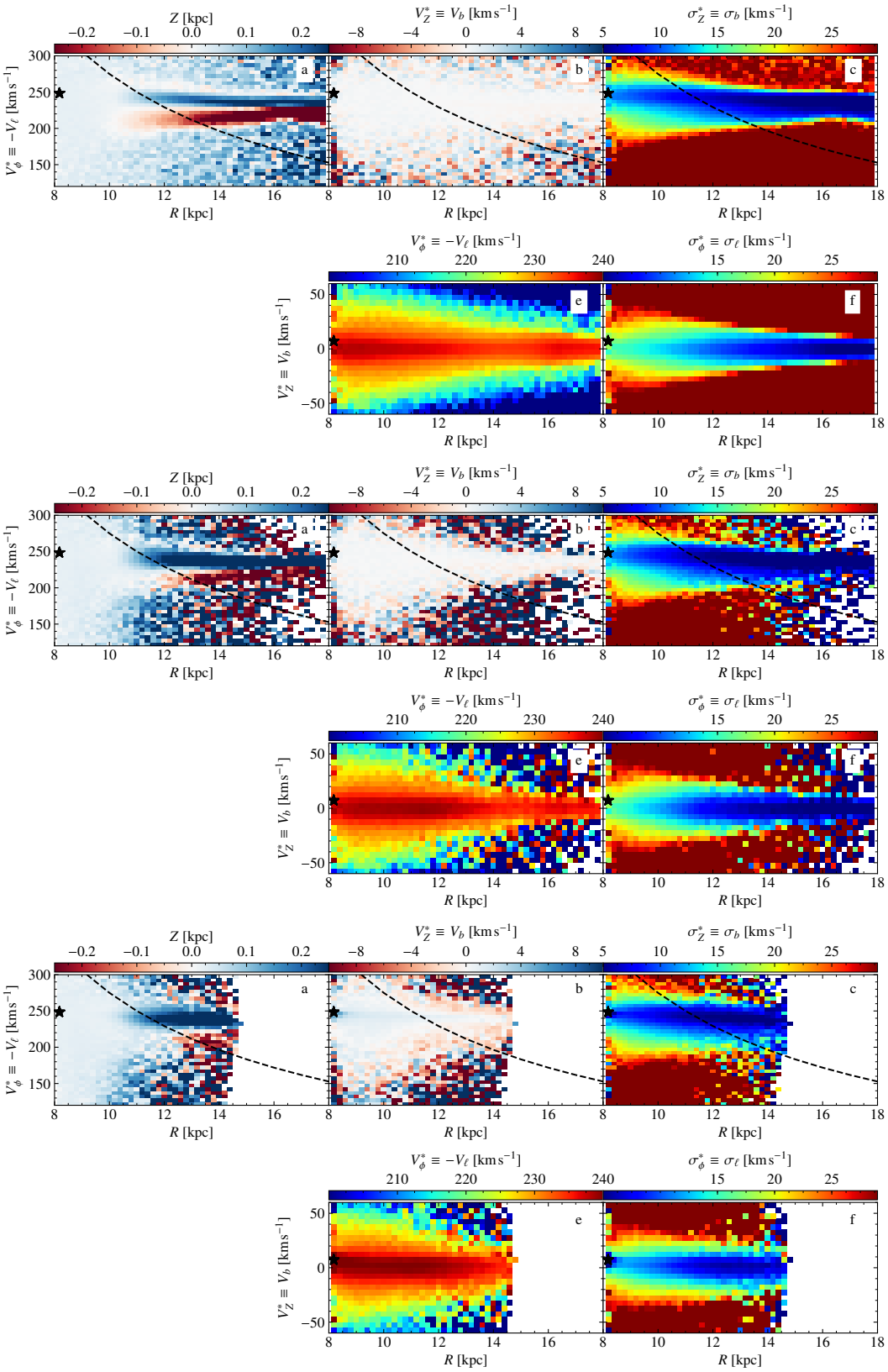

Fig. E.6. Phase space projections for model and mock data. Same as Fig. 14 but for the UM (*top*), the UM with the sources that in GOG have $\varpi/\sigma_\varpi > 3$ (*middle*), and for GOG with the selection $\varpi/\sigma_\varpi > 3$ (*bottom*). The phase space spiral does not exist in GOG and panels d are not shown.

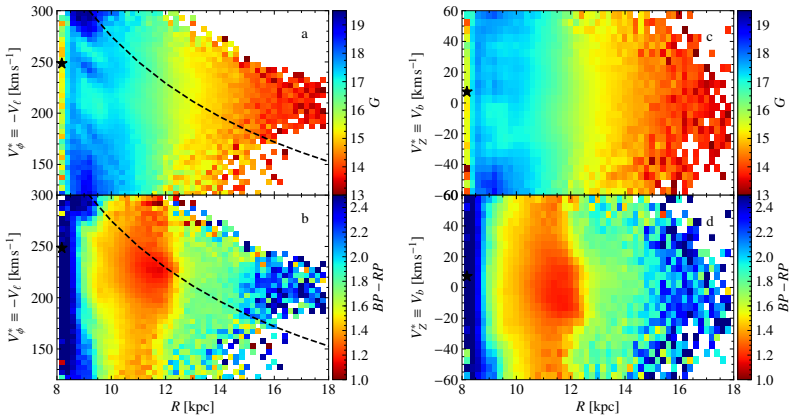

Fig. E.7. Photometry in different phase space projections. Median magnitudes G (*top*) and colour $BP - RP$ (*bottom*) in the R-V^*_ϕ plane (*left*) and R-V^*_Z plane (*right*) for the AC20-$\varpi/\sigma_\varpi > 3$ sample.

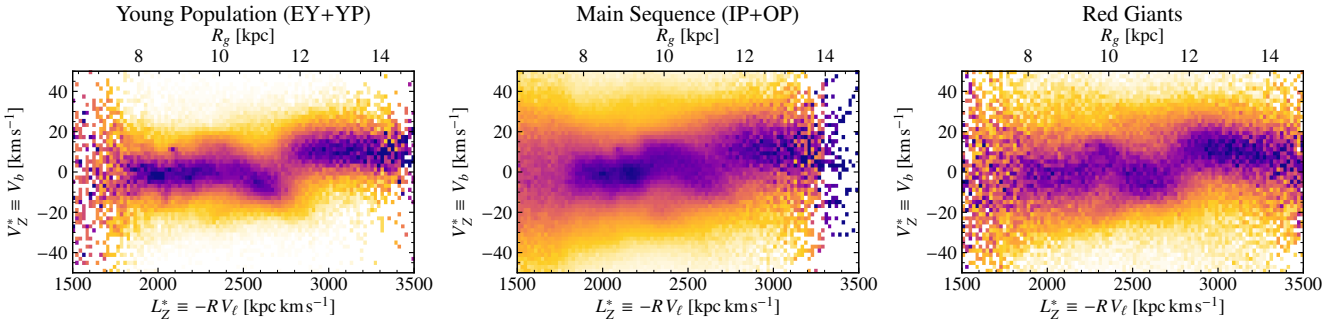

Fig. E.8. Structures in the vertical velocity and angular momentum space for different populations. As in the top panel of Fig. 15, these show a column normalised histogram of star numbers in the L^*_z, V^*_Z plane but for a given population (as in Sect. 2.2). In all cases the feature at ∼2750 km s^{-1} kpc is clearly visible. The young population has the lowest velocity dispersion, and therefore shows the feature most cleanly.